



Turbulent flow topology in supersonic boundary layer with wall heat transfer

Mostafa Safdari Shadloo, Sushank Sharma, A. Hadjadj

► To cite this version:

Mostafa Safdari Shadloo, Sushank Sharma, A. Hadjadj. Turbulent flow topology in supersonic boundary layer with wall heat transfer. International Journal of Heat and Fluid Flow, 2019, 78, pp.108430. 10.1016/j.ijheatfluidflow.2019.108430 . hal-02189352

HAL Id: hal-02189352

<https://hal.science/hal-02189352>

Submitted on 25 Oct 2021

HAL is a multi-disciplinary open access archive for the deposit and dissemination of scientific research documents, whether they are published or not. The documents may come from teaching and research institutions in France or abroad, or from public or private research centers.

L'archive ouverte pluridisciplinaire **HAL**, est destinée au dépôt et à la diffusion de documents scientifiques de niveau recherche, publiés ou non, émanant des établissements d'enseignement et de recherche français ou étrangers, des laboratoires publics ou privés.



Distributed under a Creative Commons Attribution - NonCommercial 4.0 International License

Turbulent Flow Topology in Supersonic Boundary Layer with Wall Heat Transfer

S. Sharma, M. S. Shadloo¹ and A. Hadjadj

*CORIA-UMR 6614, CNRS-University, INSA of Rouen and Normandie University,
France*

Abstract

Direct numerical simulations (DNS) are performed for the supersonic boundary layers (SBLs) with a free-stream Mach number $M_\infty = 2.2$. Different cases including the adiabatic and the isothermal (cooled and heated) walls are investigated. The laminar boundary layer is excited by means of a blowing and suction strip with single-frequency and multiple spanwise wave-numbers. The incoming laminar flow is strongly perturbed with a perturbation intensity of 2.4% of the free-stream velocity to obtain the turbulent boundary layer. In the fully developed turbulent regions, the joint probability density function (JPDF) distribution and the covariance integrands' analyses of different parameters are performed to find out the contribution of various physical mechanisms towards different transfer processes. The results reveal that behavior of the turbulent shear stress is similar to its incompressible counterpart and the wall-temperature impacts are dominant in the buffer layer region (at $y^+ = 10$). The inclination angles of coherent structures show variations arising from the wall-temperature in both the buffer-layer and the

¹Email for correspondance: msshadloo@coria.fr

log region. The covariance integrands' analyses of different components of the heat flux reveal the dominance of a different transfer process in case of the cooled wall, and as a result of this difference, the cooled wall acts as a heat sink.

Keywords: Supersonic boundary layer, Turbulent flow, Direct numerical simulation (DNS), Joint Probability Distribution Function (JPDF) distribution, Covariance integrand analysis

1. Introduction

An increasing focus towards the improvement in the designs of the supersonic aircraft, calls for a better understanding of the high-speed flows. Various other applications such as the flow through a supersonic propulsive nozzle [1], demand for better characterization of the supersonic turbulent boundary layers. Due to the complexity posed by the compressibility effects in case of the high-speed flows, it therefore becomes necessary to explore the implications of different physical parameters such as the surface temperature on the flow itself [2].

The scientific community is trying to characterize the turbulent flows from a very long period of time. The study performed by Theodorsen [3] brings out the importance of the coherent structures in case of the incompressible turbulent wall-bounded flows. Their results shed light on the fact that these structures are responsible for low-momentum fluid transport and Reynolds shear-stress production. The morphology of these structures were experimentally verified by Head and Bandyopadhyay [4]. The investigation presented in [5] suggests that in the turbulent boundary layer, the asymmetric

18 one-legged hairpin vortex is the most-probable shape of the coherent struc-
 19 tures. Later on, the numerical study performed by Wu and Moin [6] stated
 20 that the forests of hairpin vortices dominate the turbulent boundary layer.
 21 Experimentally, the events of ejections and sweeps which are responsible
 22 for Reynolds shear-stress production were visualized by Corino and Brod-
 23 key [7]. Wallace et al. [8] quantified the turbulent processes and provided
 24 further insight about Reynolds stress production in the near-wall region for
 25 the incompressible turbulent channel flows. Their results reveled that ejection
 26 tions and sweeps together contribute more than 100% to the Reynolds stress,
 27 and the additional stress was countered by other contributing factors named
 28 interactions.

29 For the incompressible turbulent channel flows, Wallace and Brodkey [9]
 30 performed the joint probability density distribution function (JPDF) and the
 31 covariance integrands' analyses for the streamwise and wall-normal velocity
 32 fluctuations in order to find out the contribution of different transport pro-
 33 cesses towards the Reynolds shear-stress. Their results suggest that when
 34 moving from the near wall-region i.e. $y^+ = 5$ to the end of the log region,
 35 different physical phenomena dominate the transfer processes. They also
 36 showed that the most-probable velocity pairs did not have the largest contri-
 37 bution towards the shear-stress. Major contribution of ejections towards the
 38 Reynolds shear stress was also reported by the experimental investigation
 39 of Willmarth and Lu [10]. The results presented by Ong and Wallace [11]
 40 highlighted the ability of the JPDF and covariance analyses in determining
 41 the topology of the turbulent flows. The results of this study helped in de-
 42 termining the most probable angles of inclination of the vorticity filaments

43 using the covariance integrands' analyses. The events of vortex stretching
 44 and compression were also discussed in detail. It was found that the average
 45 stretching of the filaments was greater than compression at all of the con-
 46 sidered locations [11]. Direct numerical simulations (DNS) of Le et al. [12]
 47 investigated the changes in three-dimensional turbulent boundary layer by
 48 employing a combination of different statistical and visualization methods.
 49 Their results uncovered that mean three-dimensionality was responsible for
 50 breaking up the symmetry and alignment of the near-wall coherent structures
 51 disrupting their self-sustaining mechanisms, and resulting in the reduction
 52 of the turbulent kinetic energy.

53 Fewer investigations have been performed so-far for the compressible tur-
 54 bulent boundary layers. For low Mach number turbulent boundary layers,
 55 the DNS results of Bechlers and Sandberg [13] found the potential backscat-
 56 ter mechanism for the transfer of the kinetic energy from smaller scales to
 57 the larger scales. The effects on the first three invariants of the velocity
 58 gradient tensor with wall-normal distance for weakly compressible flow are
 59 studied by [14]. The experimental database available for the compressible
 60 problems is scarce due to the difficulty in measurements. The experimental
 61 investigation of Spina et al. [15] revealed that the compressibility has little
 62 impact on the statistical properties of the flow. One of the first investigations
 63 reported by Morkovin [16] suggests that the effects of compressibility on tur-
 64 bulence are due to the variations of the thermodynamic properties across the
 65 boundary layer. The experimental data also confirms that the supersonic
 66 boundary layers bear close similarities to the incompressible ones [17, 18]. Li
 67 and Xi-Yun [18] have reported that the angles of inclination of the vortical

68 structures with the streamwise direction increases from sub-layer to buffer
 69 layer and then decreases from the buffer layer to the wake region. Maeder
 70 et al. [19], Pirozzoli et al. [20] have investigated the structural characteris-
 71 tics of the supersonic turbulence and found the presence of the organized
 72 motions in the outer layer. The study presented in [21] tried to quantita-
 73 tively characterize the statistical features of the coherent structures for the
 74 case of turbulent supersonic boundary layer and found that the inner layer
 75 was mostly populated by the quasi-streamwise vortices while the outer layer
 76 (including the log and the wake regions) was populated by different types of
 77 structures such as the hairpin vortices and the hairpin packets.

78 The careful examination of the existing scientific literature reveals that the
 79 studies pertaining to the effects of wall heat-transfer on turbulent flow topol-
 80 ogy for the compressible supersonic boundary layer are scarce (almost none
 81 for the heated wall). The study investigating the supersonic cooled turbulent
 82 channel flows in [22] deals with the effects of compressibility on the pressure-
 83 strain correlation and the dissipation rate tensors in the Reynolds stress
 84 budgets. The results of this study revealed that the fluctuations conditioned
 85 on ejections and sweeps in the wall-layer were instructive, and showed that
 86 the positive temperature fluctuations were mainly due to sweeps in case of
 87 the cooled wall. Moreover, the comparison with the incompressible flow data
 88 underlined that the compressibility effects persisted in the wall-layer only.
 89 Relevant statistical properties of the compressible turbulent flows (including
 90 the heated wall) are assessed in [23]. This study found that the Morkovin's
 91 hypothesis was neither valid for the heated walls nor for the cooled walls. The
 92 analysis of the turbulent kinetic energy budget showed that the dilatational

93 to solenoidal dissipation ratio increases/decreases with heating/cooling of the
 94 wall. Later on, Trettel and Larsson [24] proposed the transformations of the
 95 velocity and the wall-coordinate simultaneously for the supersonic isother-
 96 mal turbulent channel flows and the turbulent boundary layers, relating the
 97 compressible mean velocity profile at any given Mach number. For low-Mach
 98 number heated channel flows, Patel et al. [25] found that the van Driest trans-
 99 formed mean temperature profiles of variable property cases collapsed with
 100 the constant property cases if the semilocal Reynolds number and the local
 101 Prandtl number distributions are constant across the channel. Chu et al.
 102 [26] studied the effects of wall temperature on the orientation of the vortical
 103 structures and other statistical properties like Morkovin’s scaling. It was
 104 found that with increasing wall-temperature, the spanwise distance between
 105 the legs of the hairpin vortex increased, the mean swirling strength and the
 106 angle of the vorticity filament with the wall also increased in the inner layer.
 107 However, the statistical properties of the vortical structures were nearly in-
 108 sensitive to the wall temperature in the outer layer. Moreover, they also put
 109 forward a new criteria for better characterizing the angles of inclination of
 110 the vortical structures. Other works characterized the factors influencing the
 111 transition scenarios for the compressible supersonic flows [27, 28, 29].

112 For the supersonic boundary layers, it is important to address the impacts
 113 of wall-heating and cooling on the arrangement and the orientation of the
 114 vortical structures, and the heat-transfer mechanisms, which are the funda-
 115 mental and still open questions for the community. In this study, the JPDF
 116 and the covariance integrands’ analyses are utilized to unravel the physical
 117 mechanisms responsible for the heat-transfer in the streamwise and the wall-

normal directions. Various quadrant analyses have been put forward to find out the most-significant and contributing transfer process responsible for the turbulent shear stress, the vortical structures' orientation and the turbulent heat-flux.

This paper is structured as follows: the governing equations and details of the computational setup including the boundary conditions are given in §2, followed by the description of the turbulent boundary layer in §3. Then a detailed discussion about the turbulent shear stress, topology of the coherent structures and different components of the turbulent heat-transfer is presented in §4.1, §4.2 and §4.3, respectively. The conclusions of the paper are presented in §5.

2. Description of the numerical setup

2.1. Governing equations

The motion of a Newtonian fluid is governed by the set of equations known as the *Navier – Stokes equations* (NSE) comprising of the equations of conservation of mass, momentum and total energy. The NSE are non-dimensionalized using the free-stream quantities and the boundary layer thickness at the inlet δ_{in}^* as the reference length:

$$\frac{\partial \rho}{\partial t} + \frac{\partial \rho u_j}{\partial x_j} = 0, \quad (1)$$

$$\frac{\partial \rho u_i}{\partial t} + \frac{\partial \rho u_i u_j}{\partial x_j} = -\frac{\partial p}{\partial x_i} + \frac{\partial \tau_{ij}}{\partial x_j}, \quad (2)$$

$$\frac{\partial \rho E}{\partial t} + \frac{\partial (\rho E + p) u_i}{\partial x_i} = -\frac{\partial q_i}{\partial x_i} + \frac{\partial u_i \tau_{ij}}{\partial x_j}, \quad (3)$$

136 where, density $\rho = \rho^*/\rho_\infty^*$, velocity $u = u^*/u_\infty^*$, time $t = t^* \times u_\infty^*/\delta_{in}^*$, pres-
 137 sure $p = p^*/(\rho_\infty^* u_\infty^{*2})$ and energy $E = E^*/u_\infty^{*2}$. Throughout this paper, the
 138 free-stream quantities are marked by the subscript ∞ and the dimensional
 139 quantities are marked by the asterisk superscript (*).

140 τ being the symmetric viscous stress tensor, which is given by:

$$\tau_{ij} = \frac{\mu}{Re} \left(\frac{\partial u_j}{\partial x_i} + \frac{\partial u_i}{\partial x_j} - \frac{2}{3} \frac{\partial u_k}{\partial x_k} \delta_{ij} \right). \quad (4)$$

141 where, viscosity $\mu = \mu^*/\mu_\infty^*$, Reynolds number $Re = \rho_\infty^* u_\infty^* \delta_{in}^*/\mu_\infty^*$ and δ_{ij} is
 142 the Kronecker delta. The pressure and the heat-flux are computed using the
 143 equation of state and the Fourier law of heat conduction respectively:

$$p = (\gamma - 1) \left(\rho E - \frac{1}{2} \rho u_i u_i \right) = \frac{1}{\gamma M_\infty^2} \rho T, \quad (5)$$

144 and

$$q = \frac{-\mu}{(\gamma - 1) M_\infty^2 Re Pr} \frac{\partial T}{\partial x_j}. \quad (6)$$

145 with temperature $T = T^*/T_\infty^*$, constant specific heat ration $\gamma = 1.4$ and
 146 Mach number $M_\infty = u_\infty^*/\sqrt{\gamma R^* T_\infty^*}$ with gas constant $R^* = 287 J/K kg^{-1}$ and
 147 Prandtl number $Pr = 0.72$.

148 The Sutherland's law has been used to calculate the dynamic viscosity:

$$\mu^*(T^*) = \frac{C_1^* T^{*3/2}}{T^* + S^*}, \quad (7)$$

149 where, $S^* = 110.4$ K is Sutherland's temperature for air and C_1^* is a constant,
 150 $1.458 \times 10^{-6} \text{ kg/ms} \sqrt{K}$ which can be written as:

$$C_1^* = \frac{\mu_r^*}{T_r^{*3/2}} (T_r^* + S^*), \quad (8)$$

151 where μ_r^* is the reference dynamic viscosity of the air, 1.716×10^{-5} kg/ms
152 at the reference temperature, T_r^* of 273.15 K. The subscript r refers to the
153 reference values.

154 2.2. Numerical solver

155 We have utilized a well validated DNS - LES numerical solver named
156 CHOC-WAVES to solve the three-dimensional, compressible, unsteady NSE
157 for perfect gases. This solver discretizes the convective fluxes by a hybrid
158 conservative sixth-order central scheme with fifth-order Weighted Essential
159 Non-Oscillatory (WENO) scheme [30, 31]. Convective terms are splitted in
160 a skew-symmetric form to minimize the aliasing error and to enforce discrete
161 conservation of the kinetic energy which results in better numerical stability.
162 Approximation of the diffusive terms is done with the fourth or the sixth
163 order formulas, and they are expanded in the Laplacian form. The time
164 integration is performed using the third-order Runge-Kutta (RK-3) scheme.
165 More details on validation can be found in ([32, 33, 34]).

166 2.3. Problem setup

167 This study utilizes the supersonic flow over a flat plate with free-stream
168 Mach number $M_\infty = 2.2$, temperature $T_\infty^* = 177$ K, pressure $p_\infty^* = 23796$
169 Pa and viscosity $\nu_\infty^* = 2.55 \times 10^{-5}$ m²/s. The choice of the Mach number
170 is based on the fact that at higher Mach numbers, the second mode insta-
171 bilities or the Mack modes [35] dominate the flow and hence the effects of
172 wall heat-transfer could not be distinguished prominently [27, 28, 29]. The
173 computational domain is free of the shocks generated at the leading edge of
174 the flat-plate because the inlet is placed downstream of the leading edge at

175 $x_{in}^* = 0.1016$ m with inlet Reynolds number $Re_{x_{in}} = 2.33 \times 10^6$ and unit
 176 Reynolds number $Re_{unit}^* = 2.293 \times 10^7/\text{m}$. The length and the height of the
 177 domain are $L_x^* = 0.15$ m and $L_y^* = 0.0127$ m respectively. The height of
 178 the computational domain is chosen such that the boundary layer thickness
 179 towards the end of the domain is approximately one-third of the height of the
 180 domain. The spanwise width of the domain is set equal to the fundamental
 181 wavelength of the excited mode i.e. $L_z^* = \lambda_z^* = 0.00605$ m corresponding
 182 to the most-unstable mode predicted by the Linear stability theory (LST)
 183 [27, 28]. Two-point correlations in the spanwise direction are plotted (not
 184 shown here) which assure that the periodicity does not affect the generated
 185 turbulence. Uniform mesh spacing is used in both the streamwise and the
 186 spanwise directions with $N_x = 4096$ and $N_z = 280$ being the number of points
 187 in the given directions. However, in the wall-normal direction ($N_y = 150$),
 188 points are more concentrated close to the wall in order to resolve the bound-
 189 ary layer. The stretching function in the wall-normal direction is given by:

$$y^* = L_y^* \frac{1 + \tanh(\kappa_o y^*)}{\tanh(\kappa_o)}, \quad (9)$$

190 with, $\kappa_o \approx 3$ being the stretch parameter.

191 Details about various DNS cases under investigation are enlisted in table
 192 1. In this table, A, C and H stand for the adiabatic, cooled and heated walls
 193 respectively. As seen in table 1, constant excitation frequency i.e. $\omega^* = 150$
 194 krad/s (or 23.87 kHz) is chosen for the blowing and suction strip for all the
 195 cases which corresponds to the most-unstable frequency according to the LST
 196 [27, 28]. Moreover, the perturbation intensity is kept high i.e. 2.4% of the
 197 free-stream velocity in order to strongly excite the boundary layer, so that

Table 1: Computational parameters for various test cases. A, C and H stand for the adiabatic, the cooled and the heated walls, respectively. Subscript *min* denotes the wall-normal spacing. Superscript ⁺ denotes the quantities in wall-units. *I* is the disturbance amplitude of blowing and suction ($I = v_{wall,max}^*/u_{\infty}^*$).

Cases	T_w^*/T_{aw}^*	$I(\%)$	ω^* (krad/s)	Δx^+	Δy_{min}^+	Δz^+
A0[27]	1.00	2.4	150	5.52	0.34	2.85
A	1.00	2.4	150	5.52	0.34	3.26
C	0.75	2.4	150	8.11	0.50	4.78
H	1.50	2.4	150	3.30	0.20	1.95

the turbulent boundary layer exists in the majority of the computational domain ($> 50\%$).

2.3.1. Boundary conditions

Figure 1 represents a schematic the computational domain and the boundary conditions. At the inlet of the domain, the streamwise and the wall-normal velocities, as well as the density profile are set to the laminar Blasius profile, without any disturbance. These profiles are calculated using a dedicated solver to obtain similarity solutions for adiabatic and isothermal compressible laminar boundary layers which utilizes the Illingworth transformation [36, 37]. The boundary layer thickness at the inlet of the domain δ_{in}^* for A, C and H cases are 4.44×10^{-4} m, 3.91×10^{-4} m and 4.86×10^{-4} m respectively. For the adiabatic case, the wall temperature $T_w^* = T_{aw}^*$ (adiabatic wall temperature), while for cooled and heated walls the temperature is set as $T_w^* = 0.75 T_{aw}^*$ and $T_w^* = 1.5 T_{aw}^*$ respectively, where $T_{aw}^* \approx 1.82 T_{\infty}^*$. T_{aw}^*

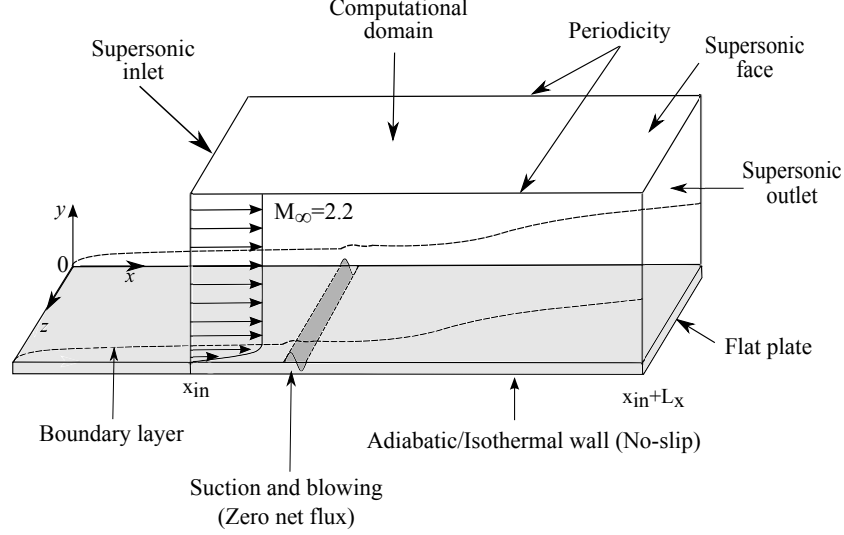


Figure 1: Computational domain and boundary conditions.

is calculated using the recovery factor approximation $Pr^{1/3}$, [36]:

$$T_{aw}^* = T_{\infty}^* \left(1 + Pr^{1/3} \times \frac{\gamma - 1}{2} \times M_{\infty}^2 \right) \quad (10)$$

Supersonic inflow and outflow boundary conditions are imposed at the inlet (x_{in}^*) and at the outlet ($x_{out}^* = x_{in}^* + L_x^*$) respectively. The side-walls of the domain are periodic and for the upper face of the domain, zero boundary-normal gradient is imposed. No-slip and no-penetration condition is used for at the surface of the wall ($y = 0$), except for the narrow strip of blowing and suction existing between $x_a^* = x_{in}^* + 0.0127$ m to $x_b^* = x_{in}^* + 0.0254$ m. The wall-normal component of the velocity in the blowing and suction strip is prescribed by the single-frequency and multiple-spanwise wavenumber boundary condition given as:

$$v^*(x, y = 0, z, t) = Iu_{\infty}^* f(x) \left[\frac{g(z)}{\max(g(z))} \right] \left[\frac{h(t)}{\max(h(t))} \right], \quad (11)$$

222

223 where I is the disturbance amplitude, $f(x)$, $g(z)$ and $h(t)$ are the streamwise,
 224 spanwise and time-dependent variations respectively, defined as:

$$f(x) = 4 \sin \theta (1 - \cos \theta) \sqrt{27}, \quad (12)$$

$$g(z) = \sum_{l=1}^{l_{max}} Z_l \sin(2\pi l(z^*/L_z^* + \phi_l)), \quad (13)$$

$$h(t) = \sum_{m=1}^{m_{max}} T_m \sin(\omega^* t^* + \phi_m). \quad (14)$$

225

226 Here, ω^* is the fundamental frequency of the induced disturbance, $\theta =$
 227 $2\pi(x^* - x_a^*)/(x_b^* - x_a^*)$, and ϕ_l and ϕ_m are the random numbers between 0
 228 and 1. The random numbers are generated using the FORTRAN subroutines
 229 of RANDOM_NUMBER and RANDOM_SEED which generate the pseudo-
 230 random numbers with uniform distribution between 0 and 1. $\sum_{l=1}^{l_{max}} Z_l = 1$,
 231 $Z_l = 1.25Z_{l=1}$, with $l_{max} = 20$ and $\sum_{m=1}^{m_{max}} T_m = 1$, $T_m = 1.25T_{m=1}$, with
 232 $m_{max} = 20$. The above mentioned methodology for generating fully devel-
 233 oped turbulent boundary layer is a modified version of the method used by
 234 Pirozzoli et al. [20]. This methodology has been used by Shadloo et al. [27]
 235 and Shadloo and Hadjadj [28], and their results present good agreement with
 236 the turbulent boundary layer results of Shadloo et al. [23] (cf. figures 4 and
 237 8 in [28]).

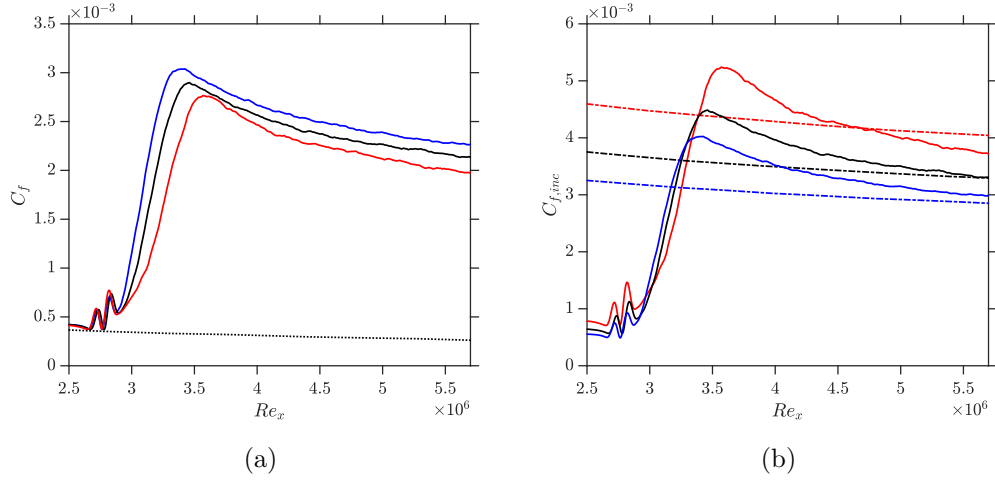


Figure 2: Streamwise evolution of (a) compressible, and (b) incompressible skin-friction coefficients as a function of Re_x for cooled (—), adiabatic (—) and heated (—) cases. Here, (.....) is $(C_{f,lam} = 0.664 \times \frac{\sqrt{\rho_w^* \mu_w^* / \rho_\infty^* \mu_\infty^*}}{\sqrt{Re_x}})$ and (—·—) is $(C_{f,inc(turb)} = 0.074 \times \sqrt{\frac{\rho_{aw}^*}{\rho_w^*}} \times Re_x^{-0.2})$ lines represent the theoretical curves for the laminar and the turbulent regimes respectively.

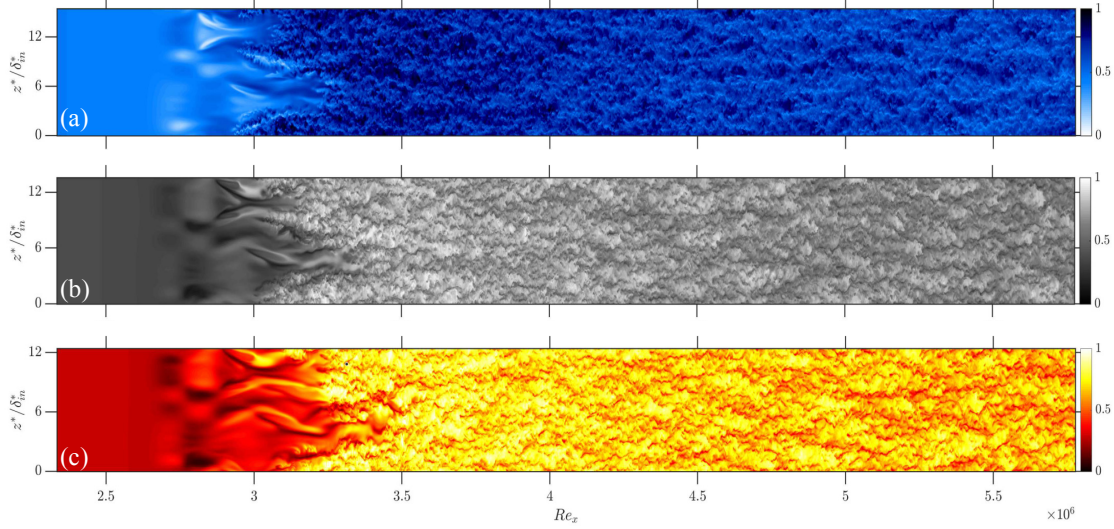


Figure 3: Instantaneous flow fields for (a) cooled, (b) adiabatic and (c) heated walls: contours of u^*/u_∞^* , shown at $y^*/\delta_{in}^* = 0.29$.

238 3. State of the turbulent boundary layer

239 Figure 2 represents the evolution of the compressible and the incompressible skin-friction coefficients C_f and $C_{f,inc}$ (averaged in time and the spanwise
240 direction) in the domain for all the cases under consideration. In this study,
241 we would regard the maximum value of C_f to mark the beginning of the fully
242 developed turbulent region. C_f can be defined as:
243

$$C_f = \frac{\tau_w^*}{\frac{1}{2}\rho_\infty^* u_\infty^{*2}} \quad (15)$$

244 where, τ_w^* is the shear stress at the wall.

245 It can be seen from figure 2a that the boundary layer begins the transition to
246 turbulence towards the end of the blowing/suction strip because of the high
247 intensity of perturbation, which sets-in the by-pass transition scenario and no

secondary instability region (usually marked by the formation of the streaks) is formed. The effect of disturbance is visible in the plot due to the high intensity of perturbation. Moreover, the levels of skin-friction coefficients rise consistently with decreasing wall-temperature in the transitional and the turbulent parts of the domain, because of the increasing local density close to the wall. More details regarding the effects of various physical parameters on the onset of transition can be found in [38, 39]. However, a contrasting trend is observed in case of the incompressible $C_{f,inc}$ (see figure 2b). These trends agree well with the findings reported by Shadloo et al. [27], Shadloo and Hadjadj [28]. Emperically, the compressible skin-friction coefficient for the laminar regime (marked by in figure 2a) is given by [36]:

$$C_{f,lam} = 0.664 \times \frac{\sqrt{\rho_w^* \mu_w^* / \rho_\infty^* \mu_\infty^*}}{\sqrt{Re_x}} \quad (16)$$

while the analytical relation for the incompressible skin-friction coefficient for the fully developed turbulent region can be given as [27]:

$$C_{f,inc(turb)} = 0.074 \times \sqrt{\frac{\rho_{aw}^*}{\rho_w^*}} \times Re_x^{-0.2} \quad (17)$$

Hence, it can be seen in figure 2a that the fully developed turbulent region starts from $Re_x = 3.42 \times 10^6$, $Re_x = 3.46 \times 10^6$ and $Re_x = 3.57 \times 10^6$ for cooled, adiabatic and heated walls, respectively. Figure 3 displays the instantaneous flow visualizations of different cases showing the existence of the turbulent region in the majority of the domain.

Frequency spectra for the adiabatic case in the middle of the domain i.e. at $z^*/\delta_{in}^* = 7$ and $y^+ = 90$ at different streamwise locations; $Re_x = 3.02 \times 10^6$, 3.94×10^6 and 5.40×10^6 along with the -5/3rd slope of turbulence decay are plotted in figure 4a-c. It can be clearly seen in these spectra plots that as we

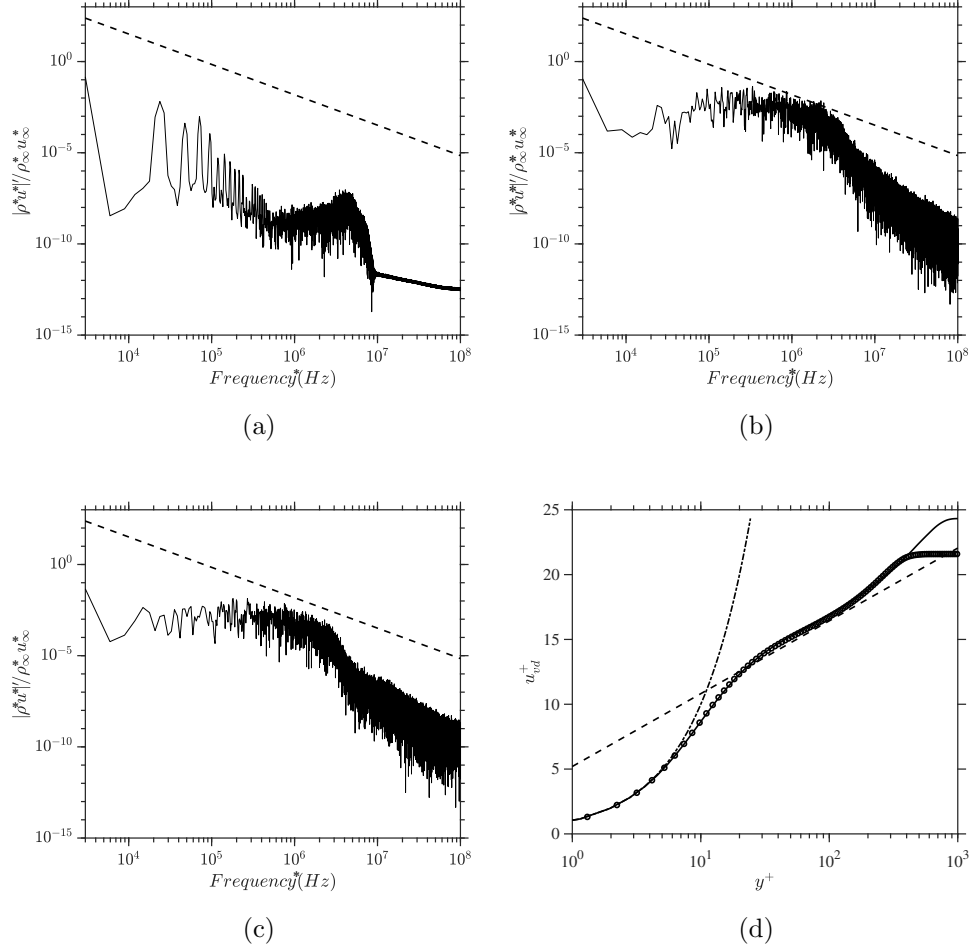


Figure 4: Frequency spectra of $|\rho^* u^{*'}|' / \rho_\infty^* u_\infty^*$ for the adiabatic wall at (a) $Re_x = 3.02 \times 10^6$, (b) $Re_x = 3.94 \times 10^6$, (c) $Re_x = 5.40 \times 10^6$; where (---) represents the $(-5/3)$ law of turbulence decay, and (d) Van-Driest transformed mean velocity profile for the adiabatic case compared with [23] (symbols) at $Re_x = 5.40 \times 10^6$, where (---) is $(1/0.41 \log y^+ + 5.2)$ and $(-\cdot-)$ is $u_{vd}^+ = y^+$.

270 move from the transition region to the fully developed turbulent regime, the
 271 excitation frequency (23.87 kHz) does no longer remain prominently visible
 272 in the frequency spectrum. Therefore, it can be stated that the resulting
 273 turbulent statistics are not affected by the forcing frequency of the blowing
 274 and suction strip. Figure 4d shows the comparison of the Van-Driest trans-
 275 formed velocity profiles at $Re_x = 5.40 \times 10^6$ for the adiabatic case vs. Shadloo
 276 et al. [23] revealing the existence of fully developed turbulent flow because
 277 the viscous sublayer and the logarithmic regions are distinctly visible.

278 **4. Joint probability density function and covariance integrands** 279 **analyses**

280 In this section, we will extensively employ the JPDF distribution and the
 281 covariance integrand analyses for investigating different properties affecting
 282 the flow topology of the supersonic turbulent boundary layers. These anal-
 283 yses would be used to describe various structural and dynamical aspects of
 284 the vortical structures and also to get a deeper insight about the physical
 285 mechanisms contributing the most to the turbulent shear-stress and the tur-
 286 bulent heat-flux. Both the JPDFs and the covariance integrands are plotted
 287 using the same bin size. It is to be noted that the results are reported for
 288 a fixed streamwise location in the fully turbulent part of the domain i.e. at
 289 $Re_x = 5.40 \times 10^6$. A grayscale color palette is used to represent the lev-
 290 els of the contours ranging from white (the **minimum** value) to black (the
 291 maximum value).

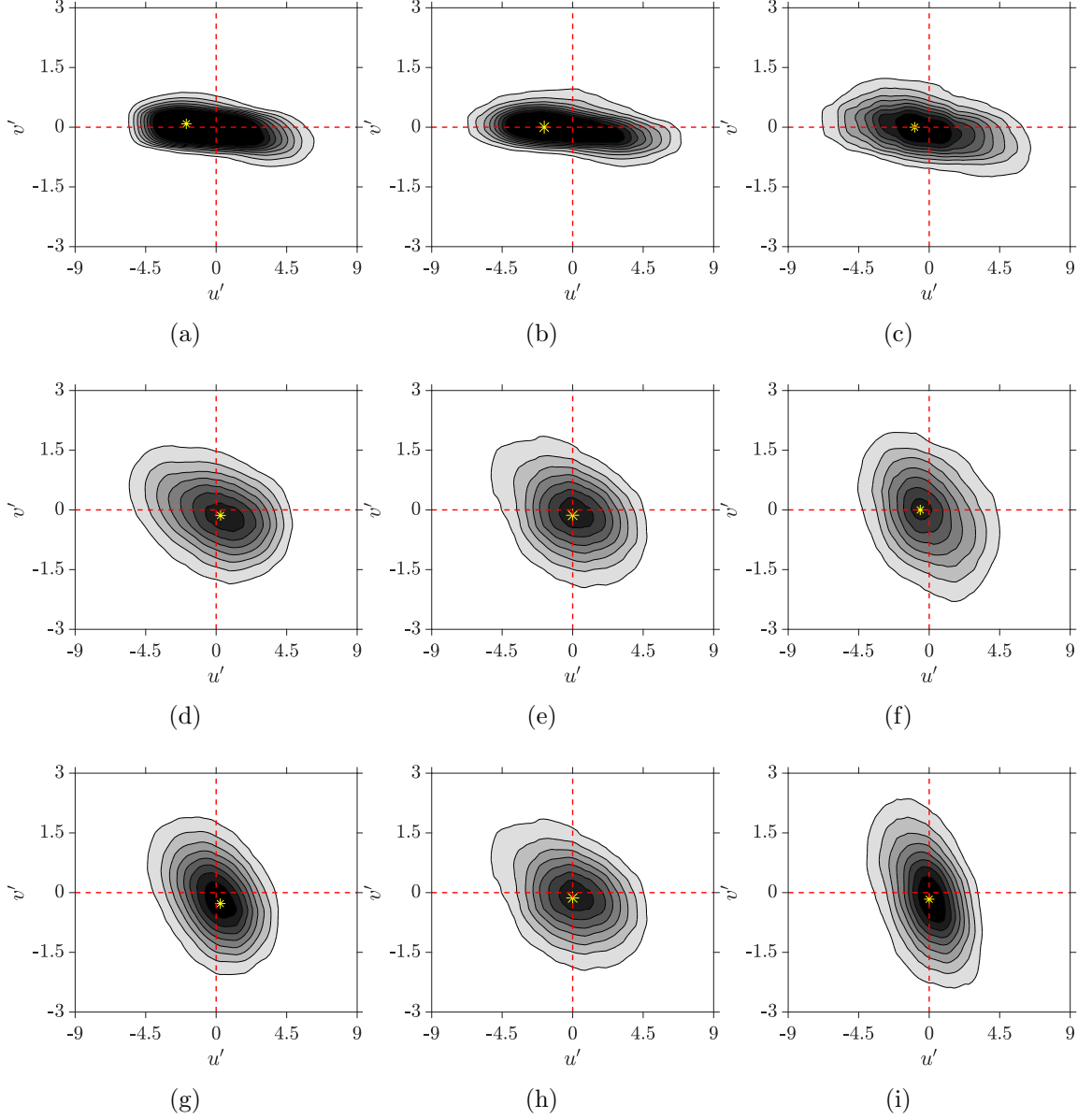


Figure 5: Contours of the joint probability density function (JPDF) distribution of the u' and v' at $y^+ = 10$ ((a)-(c)), 35 ((d)-(f)) and 90 ((g)-(i)). The colors of the contour levels vary from 1 to 8 (light to dark). Here the first, second and third columns represent the cooled, adiabatic and heated walls, respectively.

Table 2: Locations of the peaks for different cases shown in figure 5. The coordinates are marked as the (u', v') tuple.

y^+	C	A	H
10	(-1.906, 0.086)	(-1.815, 0.000)	(-0.926, 0.000)
35	(0.280, -0.139)	(0.000, -0.135)	(-0.571, 0.000)
90	(0.264, -0.276)	(0.000, -0.142)	(0.000, -0.166)

292 4.1. Velocity fluctuations

293 Figure 5 depicts the contour plots of the JPDF distribution of the fluc-
294 tuations of the streamwise (u'^*) and wall-normal (v'^*) velocity components
295 scaled by the local friction velocity $u_\tau^* = \sqrt{\tau_w^*/\rho_w^*}$ at various y^+ locations. In
296 this figure, $u' = u'^*/u_\tau^*$ and $v' = v'^*/u_\tau^*$. Table 2 enlists the peak locations
297 for the cases mentioned in the figure 5 (marked by the yellow *). The JPDF
298 contours point out that the distribution of the v' is confined to a very small
299 area in the buffer layer i.e. $y^+ = 10$, hence, the distribution is quite flat
300 (figures 5a-c). A comparison of the figures 5a-c shows that, for the near-wall
301 region, the peak tends to move towards zero (see first row of table 2) with
302 increasing wall-temperature confirming the presence of the accelerated flow
303 due to the increase in the momentum transfer process. Moreover, the peak
304 locations marked in the first row of table 2 show negligible effects of the wall-
305 temperature on the v' which is due to the strong viscous forces close to the
306 wall. Similar behavior has been reported by Wallace and Brodkey [9] in case
307 of the incompressible turbulent boundary layer. The comparison of the first
308 and the second rows of the figure 5, reveals that on moving from the buffer
309 layer to the log-region i.e $y^+ = 10$ to 35, the peak moves in the direction of

310 the fourth quadrant which means that an increasing amount of fast moving
 311 flow going towards the wall (more details on the quadrant analysis will fol-
 312 low subsequently). However in the log-region, at $y^+ = 90$ (figures 5g-i), the
 313 positions of the peaks do not show a prominent variation (also see the third
 314 row of table 2) with respect to the wall-temperature. This means that the
 315 effects of the wall-temperature are confined to the near-wall region only. On
 316 comparing figures 5d to 5f with figures 5g to 5i, it can be observed that the
 317 distribution of v' grows more rapidly and dramatically with increase in y^+ as
 318 the wall temperature increases. This trend of growth mechanism shows an
 319 increased amount of wall-normal fluctuations in the log region with increasing
 320 wall-temperature, which generates higher levels of the turbulent shear-stress
 321 in the heated case. It should be noted here that the JPDF distribution tends
 322 to align its major axis with the corresponding dominant quadrants. From
 323 our discussion of this set of figures, it can be said that impact of wall heat
 324 transfer on the distribution of u' and v' can be seen predominantly in the
 325 buffer layer region.

326 In order to have a better insight about the flow topology, we would now
 327 use the quadrant analysis previously reported in [8, 9, 10]. The quadrant
 328 analysis of the contour plots of the covariance integrands provides a better
 329 understanding of various physical phenomena related to the corresponding
 330 quantities. Each quadrant represents a particular transfer process and the
 331 dominant quadrant represents the most influential of these. The turbulent
 332 shear-stress covariance, $\overline{u'v'}$ can be written as

$$\overline{u'v'} = \int \int_{-\infty}^{\infty} u'v'P(u',v')du'dv', \quad (18)$$

333 where, $P(u',v')$ is the joint probability density function of the u' and v' over

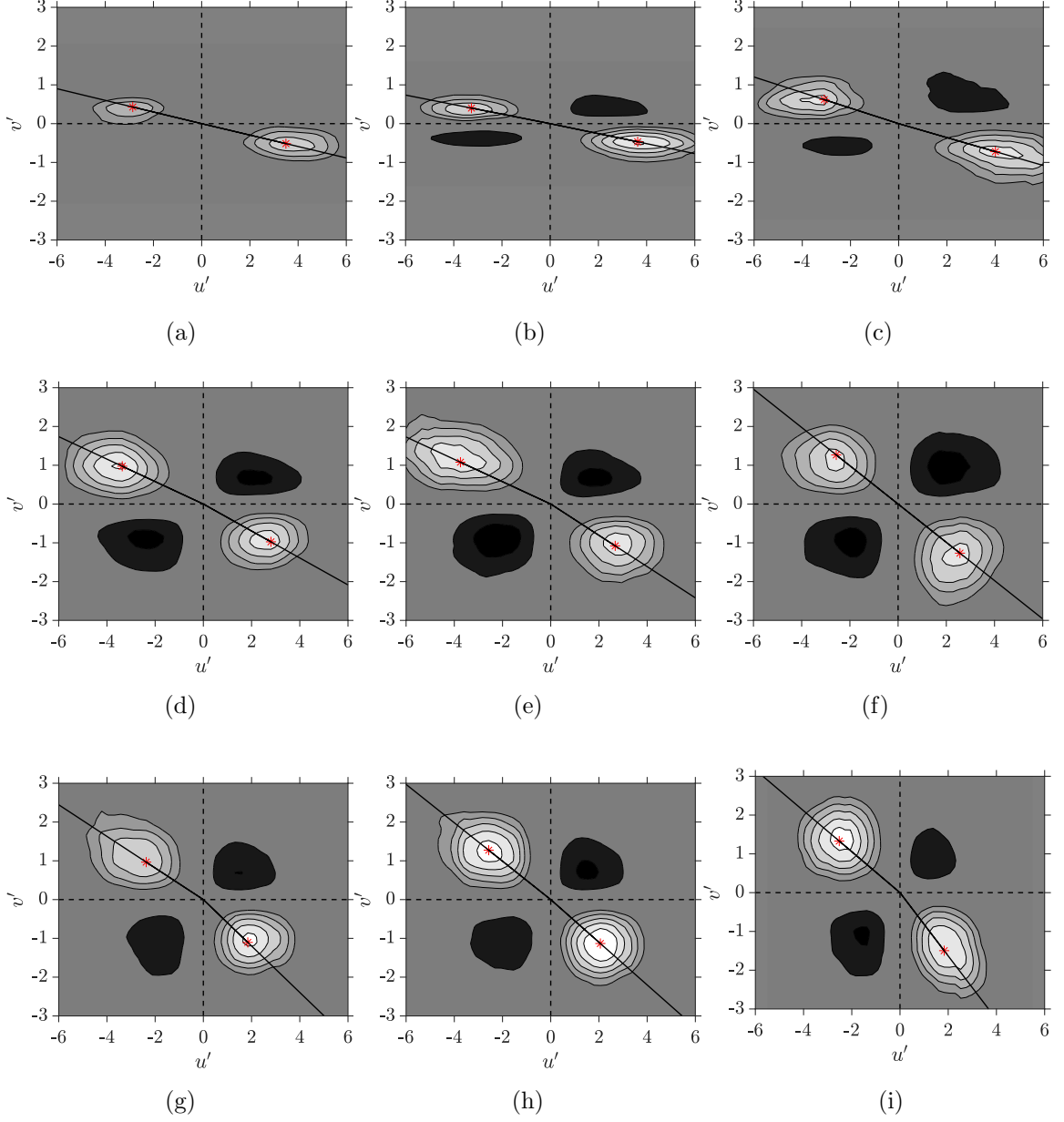


Figure 6: Contours of the covariance integrands of the u' and v' at $y^+ = 10$ ((a)-(c)), 35 ((d)-(f)) and 90 ((g)-(i)). The colors of the contour levels vary from -8 to 2, excluding the zero level (light to dark). Here the first, second and third columns represent the cooled, adiabatic and heated walls, respectively.

334 a bin area of $du'dv'$ and the quantity $u'v'P(u'v')$ is known as the covariance
 335 integrand.

336 The contour plots of the covariance integrands of $u'v'$ represent the con-
 337 tribution of signs and magnitude of a given component of velocity i.e. u' or v'
 338 towards the turbulent shear-stress covariance, $\overline{u'v'}$. The first quadrant (Q_1),
 339 where $u' > 0$ and $v' > 0$, represents the outward interactions. The second
 340 quadrant (Q_2), where $u' < 0$ and $v' > 0$, represents the events of ejections.
 341 The third quadrant (Q_3), where $u' < 0$ and $v' < 0$, represents the inward
 342 interactions, and the fourth one (Q_4), with $u' > 0$ and $v' < 0$, represents the
 343 sweeps [9, 10, 18].

344 Figure 6 represents the contour plots of the covariance integrands of the u'
 345 and v' for the corresponding y^+ positions mentioned in figure 5. In this figure,
 346 dark **contours** signify the positive contour levels i.e. **levels 1 and 2** while
 347 the light ones are the negative contour levels (**levels -8 to -1, see figure 5**).
 348 The solid black lines in each plot serve as a visual reference for determining
 349 the angles of inclination with respect to the positive u' axis. These lines
 350 originate from the origin and pass through the peaks of the most dominant
 351 quadrants (marked by the red *). The changes in the angles of inclination
 352 quantify the shift in the observed physical phenomenon for the corresponding
 353 quadrant. At a glance of figure 6, it can be said that for all of the cases
 354 Q_2 and Q_4 are the dominant quadrants which means that the ejection and
 355 sweep mechanisms contribute the most to the turbulent shear stress. **For**
 356 **incompressible channel flows, as per the findings of Wallace et al. [8], the**
 357 **ejections and sweeps contribute more than 100% towards the shear-stress,**
 358 **and additional stress generated is countered by the positive and negative**

359 interactions represented by the events of Q_1 and Q_3 respectively. Hence, the
 360 results shown in figure 6 are in good agreement with their incompressible
 361 counterparts. A closer look to this figure reveals that in the buffer region,
 362 at $y^+ = 10$, the sweeps are more important in comparison to the ejections
 363 in case of the cooled and to some extent for the adiabatic wall (figures 6a
 364 and b) because there exists an additional lower contour level. This means
 365 that the high-speed fluid moving towards the wall is the major contributor
 366 to the turbulent shear-stress. However, figure 6c suggests that for $y^+ = 10$,
 367 the ejections and sweeps become comparable for the heated wall. Therefore,
 368 it can be said that in the buffer-region, decrease in wall-temperature favors
 369 the sweep events. At $y^+ = 35$ (figures 6d-f), it can be seen that the ejection
 370 events are dominant for the cooled and the adiabatic walls, whereas for the
 371 heated wall, both the ejections and sweeps become comparable, which means
 372 that the decreasing wall-temperature favors the ejections. Towards the end
 373 of the log-region, at $y^+ = 90$, the ejections and the sweeps are comparable for
 374 the cases A and H while for the case C sweeps contribute the most towards
 375 the shear-stress covariance.

376 4.2. Vorticity fluctuations

377 In this section we would talk about the topology and the physical ori-
 378 entation of the coherent structures in the flow field. The JPDF and the
 379 covariance integrand contours of the vorticity components shed some light
 380 on the flow topology. The alignment of these contours indicates the most-
 381 likely orientation of the projections of the coherent structures at that given
 382 position in different planes. It should be noted here that this representation
 383 is global in nature and reveals the most-likely inclinations of the projections

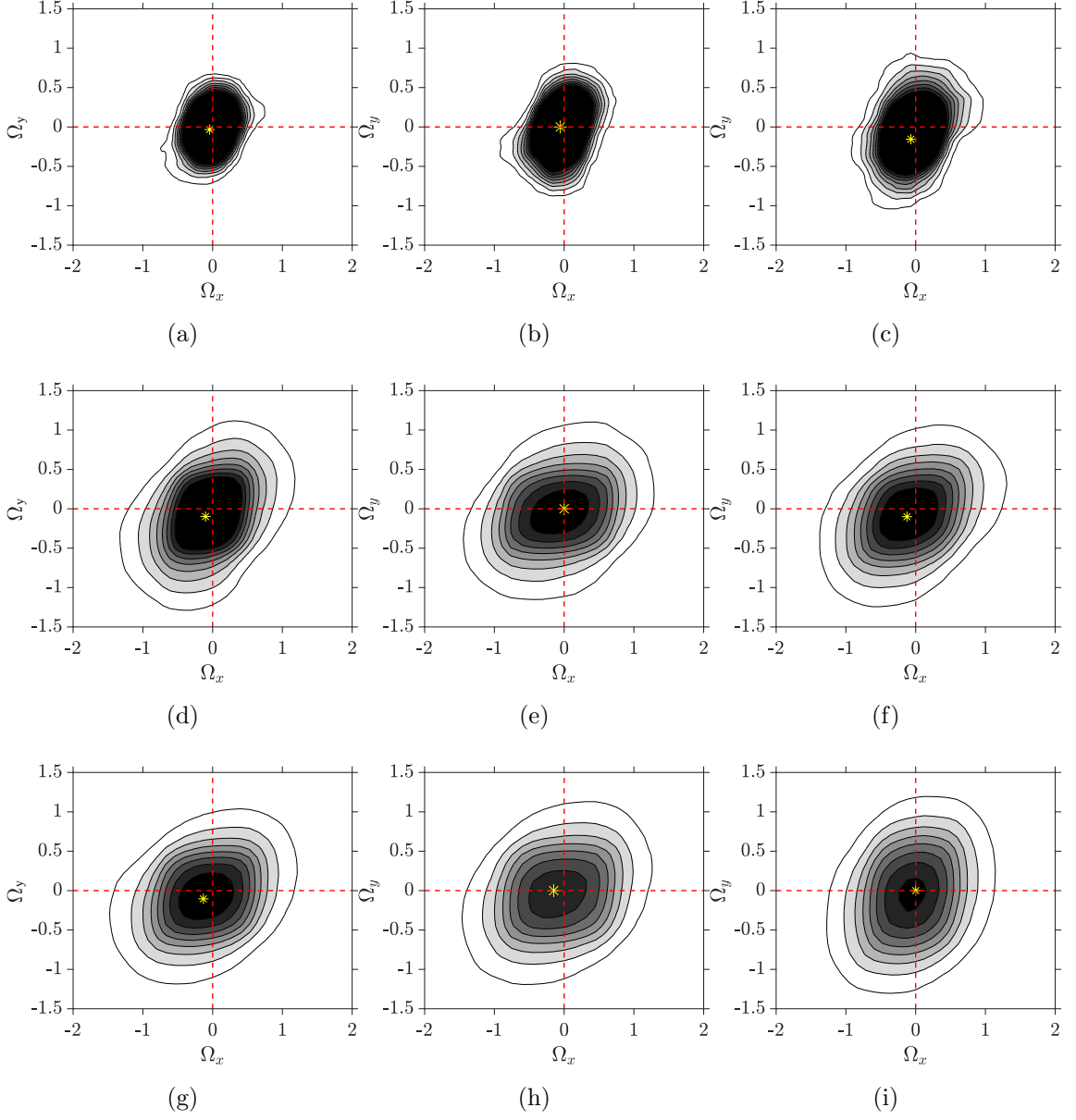


Figure 7: Contours of the JPDF distribution of the Ω_x and Ω_y at $y^+ = 10$ ((a)-(c)), 35 ((d)-(f)) and 90 ((g)-(i)). The colors of the contour levels vary from 5 to 40 (light to dark). Here, the first, second and third columns represent the cooled, adiabatic and heated walls, respectively.

384 of the coherent structures in three-dimensional sense. The structures present
 385 in the turbulent field can have any sense of rotation or they may exist in
 386 pairs of counter-rotating vortices which in three-dimensional sense represent
 387 a hairpin (or lambda) structure. Other possibilities of flow configuration also
 388 exist such as the hairpin forests [6], or the cane structures (or asymmetrical
 389 hairpins) [18] among others.

390 Figure 7 displays the contours of the JPDF distribution of the streamwise
 391 and wall-normal vorticity components; Ω_x^* and Ω_y^* respectively which are
 392 normalized by the local vorticity magnitude i.e. $\Omega_x = \Omega_x^*/\Omega^*$ and $\Omega_y =$
 393 Ω_y^*/Ω^* , where $(\langle\Omega^*\rangle = \sqrt{\Omega_x^{*2} + \Omega_y^{*2} + \Omega_z^{*2}})$, $\langle\cdot\rangle$ represents local time-averaged
 394 quantity, and $\Omega_x^* = \frac{\partial w^*}{\partial y^*} - \frac{\partial v^*}{\partial z^*}$, $\Omega_y^* = \frac{\partial u^*}{\partial z^*} - \frac{\partial w^*}{\partial x^*}$ and $\Omega_z^* = \frac{\partial v^*}{\partial x^*} - \frac{\partial u^*}{\partial y^*}$. These
 395 contours represent the most probable projections of the coherent structures
 396 in the streamwise-wall-normal plane (x-y plane) at some angle to the wall
 397 that can vary along the length of the vortical structure [11]. The orientation
 398 of these contours shows the positive correlation between the two quantities
 399 which is obvious due to the high-speed of the flow in the streamwise direction.
 400 On comparing the first, second and third rows of figure 7 it can be stated that
 401 the contours' orientation **increases** in the streamwise direction which is due
 402 to the increment in the streamwise velocity with increasing y^+ . Moreover,
 403 it can be seen from these figures that the wall-temperature does not has
 404 significant impact on the inclination of the contours.

405 The contours of the covariance integrands of Ω_x and Ω_y i.e. $\Omega_x\Omega_yP(\Omega_x, \Omega_y)$
 406 are shown in figure 8. It should be noted that, for this quadrant analysis,
 407 the physical significance of each quadrant is not the same as stated before
 408 for figure 6. In this case, the dominant quadrants highlight the most-likely

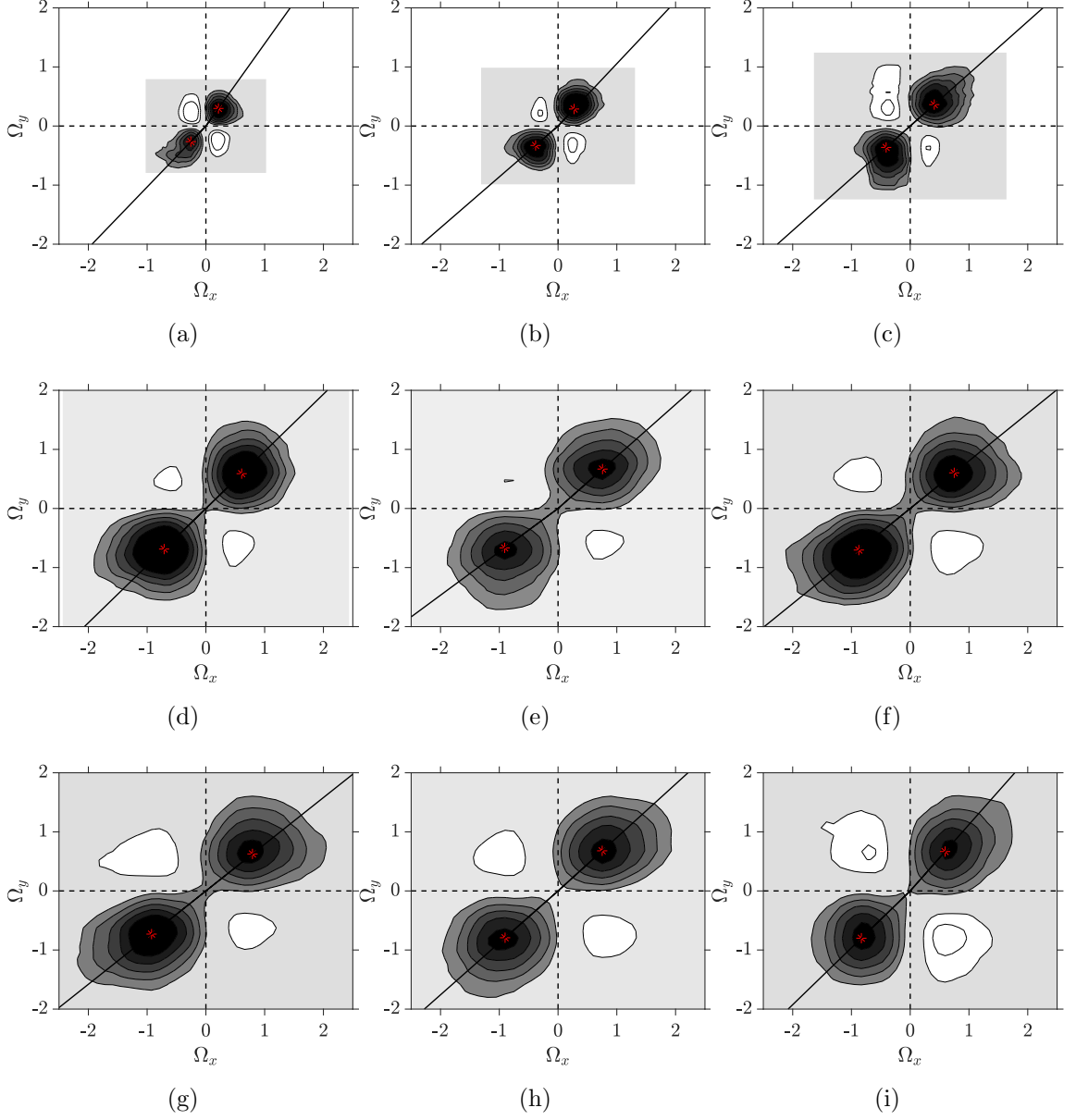


Figure 8: Contours of the covariance integrands of the Ω_x and Ω_y at $y^+ = 10$ ((a)-(c)), 35 ((d)-(f)) and 90 ((g)-(i)). The colors of the contour levels vary from -0.5 to 3, excluding the zero level (light to dark). Here the first, second and third columns represent the cooled, adiabatic and heated walls, respectively.

orientation of the vorticity filaments (their projections) at the given locations which contribute to the covariance $\overline{\Omega_x \Omega_y}$. It can be clearly seen from these plots that as a result of the positive correlation between the two quantities, Q_1 and Q_3 are the dominant quadrants here. The orientation of the projections of the vorticity filaments in the (x-y) plane can be given as

$$\alpha = \tan^{-1} \left(\frac{\Omega_y}{\Omega_x} \right) \quad (19)$$

α is the angle made by the peaks of the dominant quadrants (Q_1 and Q_3 here) with respect to the positive Ω_x -axis. The solid black lines are marked to serve as a visual aid to estimate the angles of inclination. In figures 8a-c, the white regions surrounding the gray rectangles are the areas with no data. On comparing the inclinations of the vorticity filaments at different y^+ positions, it can be observed that α is 54° , 44° and 38° in Q_1 and -134° , -136° and -142° in Q_3 for $y^+ = 10, 35$ and 90 , respectively for the cooled wall (i.e. figures 8a, d and g). This trend suggests that on moving from the buffer layer ($y^+ = 10$) to the log region ($y^+ = 35$), the filaments tend to rotate in the streamwise direction. The same trend is observed for all the three cases when moving from $y^+ = 10$ to 35 (see first two rows of table 4). However, for the adiabatic wall, the α is about 46° , 41° and 42° in Q_1 and -139° , -144° and -139° in Q_3 respectively. Hence, the adiabatic wall shows subtle variation in the log-region (angles in Q_1), this trend is similar to the one reported by Ong and Wallace [11] for the incompressible turbulent flows (keeping in mind the $\pm 5^\circ$ error for the bin size used by them). The visual inspection of the orientation and dominance of the quadrants with the literature reveals that the results of both the cooled as well as the adiabatic walls bear close similarities with the results of the compressible flows [26] (due to the different

Table 3: Locations of the peaks for different cases shown in figure 9. The coordinates are marked as the (Ω_x, Ω_z) tuple.

y^+	C	A	H
10	(0.000, -0.983)	(0.000, -0.884)	(-0.068, -0.889)
35	(-0.102, -0.497)	(0.000, -0.398)	(-0.125, -0.456)
90	(-0.132, -0.304)	(-0.150, -0.286)	(-0.119, -0.348)

433 y^+ locations reported, a direct comparison is not possible). However, for the
434 heated wall, the inclination angles decrease in the early log region followed
435 by a strong increase i.e. 42° , 39° and 48° in Q_1 for $y^+ = 10$, 35 and 90,
436 respectively. This variation in the trend of inclination means that in the log
437 region the wall-normal vorticity component is still on the rise due to increased
438 heat-transfer from the wall. A comparison between the angles of inclination
439 of the second and the third rows of figure 8 (see table 4) reveals that on
440 moving from $y^+ = 35$ to 90, the vortical filaments tend to orient themselves
441 lesser in the streamwise direction (as evident from the increasing values of α)
442 with increasing wall-temperature. Therefore, from our discussion of about
443 this set of figures, it can be stated that the wall temperature affects the usual
444 orientation of the vorticity filaments in the buffer-layer region as well as in
445 the log-region due to the strong heat transfer.

446 Now, we consider the orientation of the projections of the coherent struc-
447 tures in the x-z plane (streamwise-spanwise plane). Figure 9 shows the JPDF
448 distribution, $P(\Omega_x, \Omega_z)$ of the streamwise and the wall-normal vorticity com-
449 ponents, Ω_x^* and Ω_z^* , respectively which are normalized by the time-averaged
450 local vorticity magnitude $\langle \Omega^* \rangle$ at different y^+ positions for all the three cases

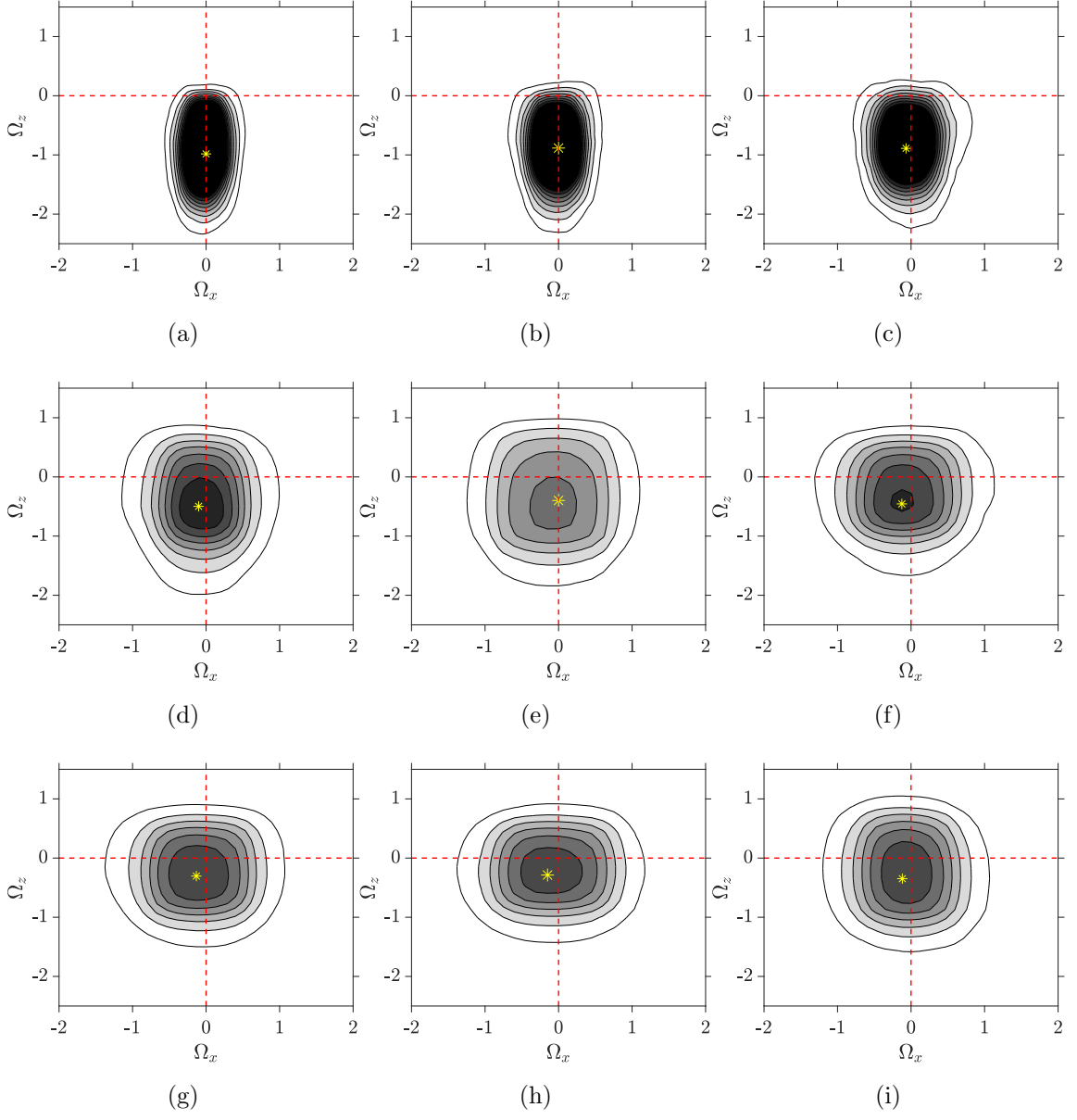


Figure 9: Contours of the JPDF distribution of the Ω_x and Ω_z at $y^+ = 10$ ((a)-(c)), 35 ((d)-(f)) and 90 ((g)-(i)). The color of the contour levels vary from 5 to 40 (light to dark). Here the first, second and third columns represent the cooled, adiabatic and heated walls, respectively.

(A, C and H), and table 3 enlists the peak locations for the same cases. It
 can be seen in these figures that in the buffer layer, $y^+ = 10$ (figures 9a to
 9c) the JPDF contours are somewhat triangular in shape. This triangular
 shape becomes predominant with increasing wall-temperature which indi-
 cates a net increase in the magnitude of Ω_x as the wall-temperature rises. As
 we progress farther from the buffer-layer region ($y^+ = 10$) to the log-region
 ($y^+ = 35$), the contours start to get more dilated in the Ω_x direction irre-
 spective of the wall-temperature, however, the peak remains in the vicinity
 of zero for the Ω_x -axis (see table 3). The dilatation of the contours gets in-
 creased with increasing wall-temperature (figures 9a to f) which means that
 increasing wall-temperature also increases the net magnitude of Ω_x . These
 triangular shapes of JPDF contours imply that the vorticity filaments do not
 show much inclination in the streamwise direction and the spanwise vorticity
 component (Ω_z) largely remains negative, meaning that it has the same sign
 as that of the mean shear. It can be clearly seen from table 3 that there
 exists a considerable shift in the location of the peak towards the positive
 Ω_z -axis ($\approx 50\%$) irrespective of the wall-temperature as one moves to the
 higher y^+ locations which implies a sudden and dramatic increase of the
 wall-normal vorticity component. This comparison of the peak location also
 reveals that the shift of the peak locations is less significant with increasing
 wall-temperature. From figure 9, it can be concluded that Ω_z is dominant in
 comparison to Ω_x because the location of the peak never changed consider-
 ably in the Ω_x -axis.

Figure 10 shows the plots of the contours of the covariance integrand of
 the Ω_x and Ω_z at different y^+ locations. The white regions around the dark

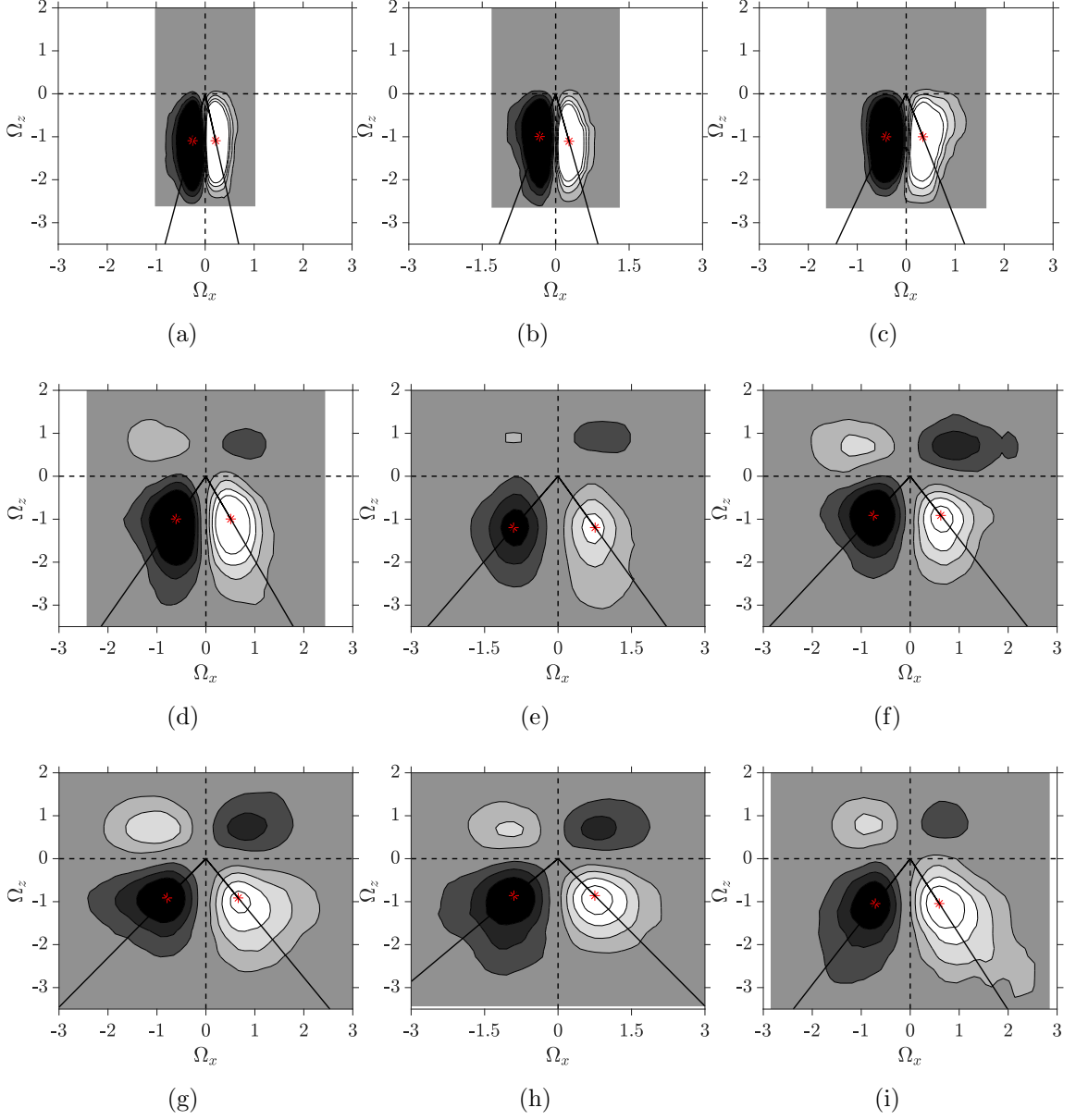


Figure 10: Contours of the covariance integrands of the Ω_x and Ω_z at $y^+ = 10$ ((a)-(c)), 35 ((d)-(f)) and 90 ((g)-(i)). The color of the contour levels vary from -2 to 1.5, excluding the zero level (light to dark). Here the first, second and third columns represent the cooled, adiabatic and heated walls, respectively.

476 rectangles in figures 10a-d and i are the regions without any data. In the
 477 buffer-layer ($y^+ = 10$, figures 10a-c), no contour levels exist in the Q_1 nor
 478 in the Q_2 which is consistent with figures 9a-c which show that the JPDF
 479 distribution of Ω_x and Ω_z exists only in the Q_3 and Q_4 . Therefore, figure
 480 10 clearly shows that the Q_3 and Q_4 are the dominant quadrants. The
 481 angles of inclination of projections of the vorticity filaments in the x-z plane
 482 (represented by the solid black lines) can be defined as

$$\beta = \tan^{-1} \left(\frac{\Omega_x}{\Omega_z} \right). \quad (20)$$

483 These inclinations are mentioned here with respect to the negative Ω_z -axis.
 484 Like before, the counter-clockwise sense is considered as the positive sense of
 485 rotation while the clockwise sense is the negative one. On moving from the
 486 buffer-layer to the log-region; from $y^+ = 10$ to 35, the inclination angles in-
 487 crease for all the cases (see table 4). Moreover, for these locations, the angles
 488 of inclination increase with increasing wall-temperature. For case C, in the
 489 buffer layer region, i.e. $y^+ = 10$ (figure 10a), the vortical filament projections
 490 are inclined at 11° and -13° in the Q_4 and Q_3 quadrants, respectively. These
 491 low values imply that in the x-z plane, the coherent structures are primarily
 492 oriented in the negative spanwise direction. However, with an increment in
 493 the distance from the wall, the filaments tend to rotate in the streamwise
 494 direction resulting in the augmentation of the angles of inclination to 27°
 495 and -31° for the Q_4 and Q_3 , respectively at $y^+ = 35$, and to 36° and -41°
 496 at $y^+ = 90$. The same trend is observed for the adiabatic wall as well (see
 497 table 4). Significant differences exist regarding the angles of inclination for
 498 the heated wall at different y^+ locations because of the increased transfer
 499 processes due to higher wall-temperature. Notably, at $y^+ = 90$, the values

Table 4: Angles of inclination of the projections of the vorticity filaments for different cases at various y^+ positions.

	Cooled wall				Adiabatic wall				Heated wall			
	α		β		α		β		α		β	
y^+	Q_1	Q_3	Q_3	Q_4	Q_1	Q_3	Q_3	Q_4	Q_1	Q_3	Q_3	Q_4
10	54	-134	-13	11	46	-139	-18	14	42	-138	-22	19
35	44	-136	-31	27	41	-144	-37	32	39	-141	-39	34
90	38	-142	-41	36	42	-139	-40	35	48	-136	-34	30

of β decrease for the heated wall (see table 4). This can be explained by the JPDP distribution shown in figure 9i, which shows a dramatic increase in the distribution of the Ω_z as a consequence of the increased wall-temperature. Hence, the distribution of Ω_x slightly shrinks. Therefore, it can be said that the wall-temperature affects the topology of the vortical elements in the x-z plane also in both the buffer-layer and the log-region.

Table 4 enlists all the values of α and β for all the cases at different y^+ positions, and also brings out the impacts of wall temperature on these angles. From this table, it can be clearly interpreted that the wall-temperature affects the turbulent flow topology in both the buffer-layer as well as the log-region for the SBLs.

4.3. Streamwise velocity component and temperature fluctuations

So far, we have discussed the kinetic aspects of the flow in detail which dealt with the velocity fluctuations and the vorticity components. For this study, we are utilizing different wall temperatures, hence, it becomes vital to investigate the implications of the wall-temperature on the heat-flux. More-

Table 5: Locations of the peaks for different cases shown in figure 11. The coordinates are marked as the (u', T') tuple.

y^+	C	A	H
5	(-1.145, -0.004)	(-1.391, 0.013)	(-1.221, 0.011)
10	(-1.906, -0.000)	(-1.815, 0.026)	(-0.926, 0.026)
35	(0.280, -0.006)	(-0.268, 0.000)	(-0.570, 0.025)
90	(-0.264, -0.006)	(0.000, -0.009)	(0.000, -0.029)

over, in the supersonic regime, the wall-temperature is one of the important factors to be looked into because it is impacted by different physical quantities like the local density and viscosity which themselves are affected by the compressibility.

Figure 11 shows the JPDF distribution of the streamwise velocity fluctuations (u'^*) and the temperature fluctuations (T'^*) for all the cases at different y^+ locations, and table 5 enlists the locations of the peaks for the corresponding cases. In this figure, an additional location in the viscous sub-layer ($y^+ = 5$) is also shown, in order to explore the near-wall region in greater detail. Here, the temperature axis is scaled by the time-averaged local temperature, $\langle T^* \rangle$ and the velocity by the local friction velocity (u_τ^*). The relation between the u' and the T' represents the turbulent heat-flux in the streamwise direction. For the rest of the manuscript, the correlation and the anti-correlation between the mentioned quantities refers to the existence of the positive, and the negative slopes respectively of the JPDF contours with the axis of abscissae. A comparison of the figures 11a to 11c highlights the effects of the wall-temperature in the viscous sub-layer. It can be

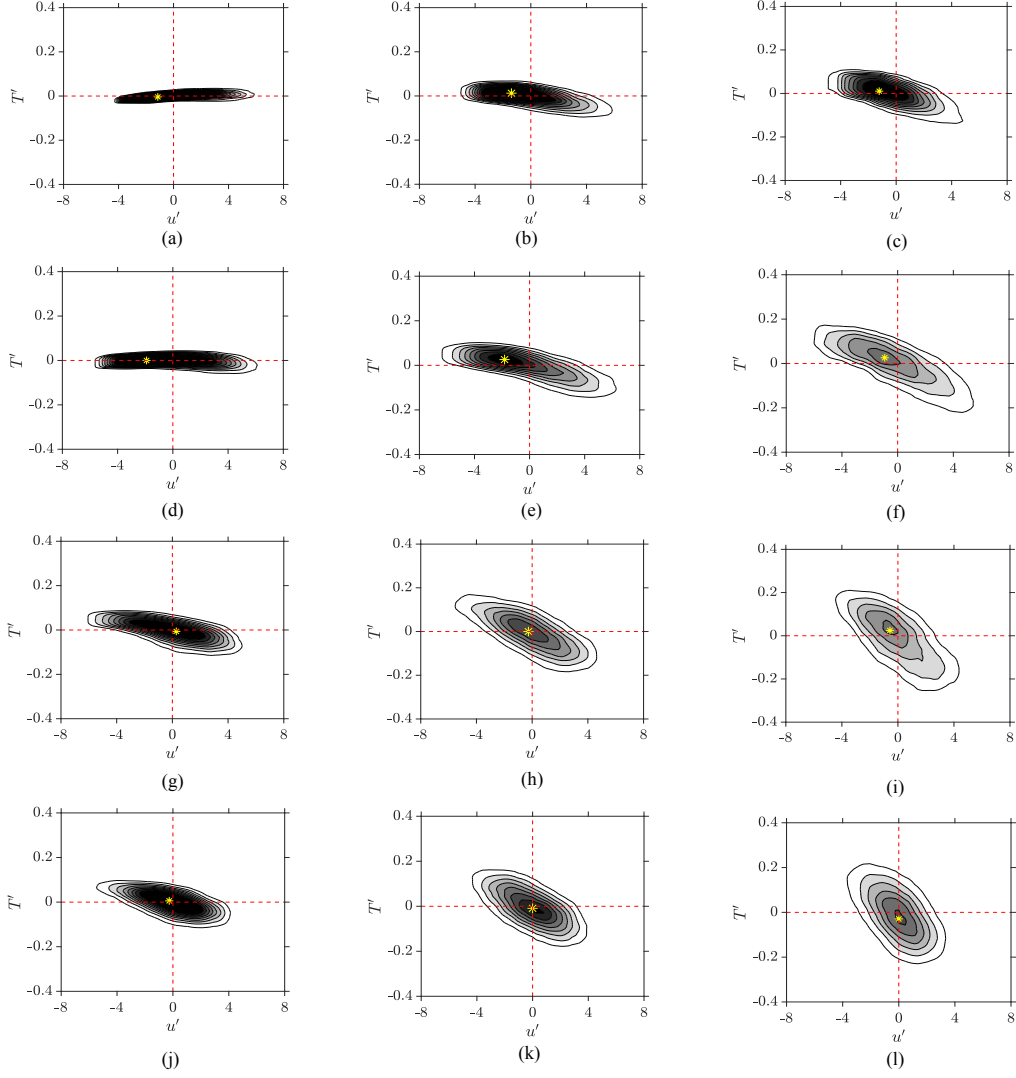


Figure 11: Contours of the JPDF distribution of the u' and T' at $y^+ = 5$ ((a)-(c)), 10 ((d)-(f)), 35 ((g)-(i)) and 90((j)-(k)). Here the first, second and third columns represent the cooled, adiabatic and heated walls, respectively. the color of the contour levels vary from 15 to 120 (light to dark).

533 seen that in case of the cooled wall, in the viscous sub-layer, the u' and T'
 534 are directly correlated, while a clear anti-correlation can be seen in case of
 535 the adiabatic and the heated walls. This trend has been reported by Duan
 536 et al. [2], Lechner et al. [22], Shadloo et al. [23] for the supersonic turbu-
 537 lent flat plates and the channel flows. This set of figures clearly reveals a
 538 trend of change in the orientation of the major axis of the JPDF contours
 539 with increment in the y^+ with respect to the u' axis. For case C, in the
 540 buffer layer region (at $y^+ = 10$), the JPDF contours become parallel to the
 541 u' axis representing a flat distribution. It can be seen from figure 11d that
 542 the peak of u' is shifted to the negative side (see first column of table 5)
 543 which implies the existence of the retarded flow in the streamwise direction.
 544 **On the other hand, the flow is comparatively less retarded for the adiabatic**
 545 **and the heated walls.** This clearly indicates that in the buffer-layer region
 546 $y^+ = 10$, the increasing wall-temperature tends to decrease the deceleration
 547 of the flow in the streamwise direction. For the higher y^+ , the u' and the T'
 548 become anti-correlated for the cooled wall. However, the adiabatic and the
 549 heated cases remain anti-correlated from the viscous sub-layer itself. It can
 550 be clearly seen from the figures 11g-l that in the log-region, for all the cases,
 551 the peak location remains very close to zero (see table 5) which indicates
 552 the existence of the homogenous turbulence. This set of figures also clarifies
 553 that the increasing wall-temperature favors the anti-correlation between the
 554 u' and the T' .

555 The contours of the covariance integrands of the u' and T' , i.e. $u'T'P(u', T')$
 556 are shown in figure 12 which represent the contributions of the u' and the
 557 T' towards the streamwise component of the heat-flux, $\overline{u'T'}$. In order to

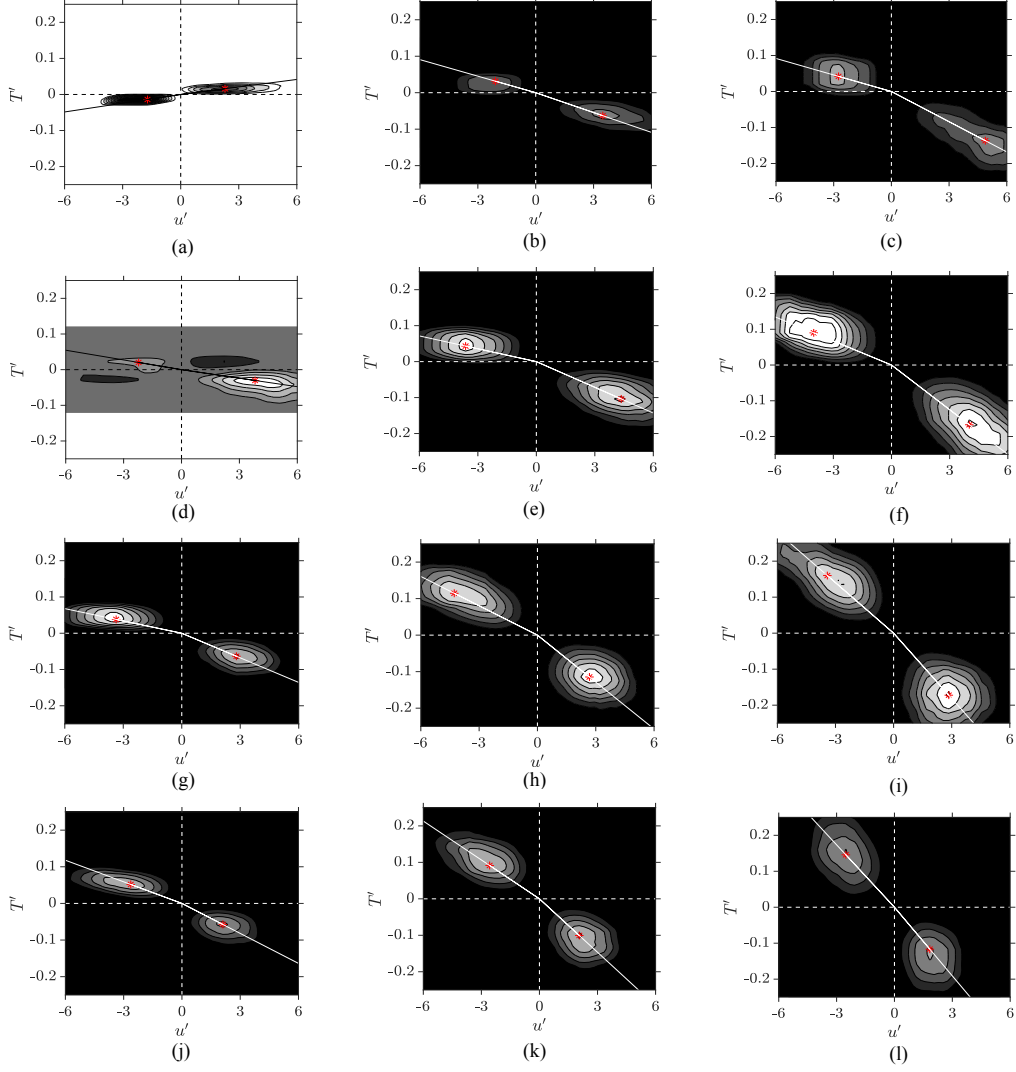


Figure 12: Contours of the covariance integrands of the u' and T' for $y^+ = 5$ ((a)-(c)), 10 ((d)-(f)), 35 ((g)-(i)) and 90((j)-(l)). Here the first, second and third columns represent the cooled, adiabatic and heated walls, respectively. The colors of the contour levels vary from 2 to 9 (light to dark) for (a), from -5 to 2, excluding the zero level for (d) and from -16 to -4 for the rest.

understand the physical phenomena responsible for this transfer process, we
 present the following quadrant analysis. The first quadrant (Q_1), where
 $u' > 0$ and $T' > 0$, indicates fast moving heated fluid. The second quadrant
 (Q_2), with $u' < 0$ and $T' > 0$, indicates slow moving heated fluid. The third
 quadrant (Q_3), having $u' < 0$ and $T' < 0$, means that the cooled fluid is
 moving slower while the fourth quadrant (Q_4), where $u' > 0$ and $T' < 0$,
 denotes the events of fast moving cooled fluid. As can be seen, in all the fig-
 ures except figure 12a where clear dominance of the Q_1 and Q_3 can be seen,
 the Q_2 and Q_4 are the dominant quadrants owing to the anti-correlation
 between the u' and T' . For the cooled wall, at $y^+ = 5$ (figure 12a), Q_3 is
 dominant in comparison to Q_1 which means that the slow moving cold fluid
 contributes more to the turbulent heat-flux in the streamwise direction than
 the fast moving hot fluid. In the buffer-layer, at $y^+ = 10$ (figure 12d), where
 the change in the inclination of the contours is registered, it can be seen that
 Q_4 is more dominant in comparison to Q_2 , highlighting the fact that fast
 moving cooled fluid has more contribution towards the streamwise turbulent
 wall heat-transfer. In case of the adiabatic and the heated walls, it can be
 seen that the major contribution comes from Q_2 than Q_4 , extending from
 the viscous sub-layer to the log region. The comparable dominance of the Q_2
 and Q_4 implies the existence of homogeneous turbulence towards the outer
 layer. It can also be observed from these figures that on moving away from
 the surface of the wall i.e. towards the higher y^+ , the angles of inclination
 of the contours also increase because of the increased perturbations. From
 this comparison we can state that for the cooled wall, the effects of wall tem-
 perature on the streamwise turbulent heat-flux can be seen from the viscous

sub-layer to the buffer-layer. And, in the log-region, the wall temperature does not has significant effects due to the turbulent mixing happening in the outer layers.

4.4. Wall-normal velocity component and temperature fluctuations

In order to have a complete overview of the heat-transfer phenomenon, we would now focus on the wall-normal component of the turbulent heat-flux which is given by the covariance of the wall-normal velocity and temperature fluctuations. The contours plots of the JPDP distribution of the wall-normal velocity fluctuations (v'^*) and temperature fluctuations (T'^*) are shown in figure 13. Here, the velocity and the temperature fluctuations are scaled by the local friction velocity (u_τ^*) and the time-averaged local temperature $\langle T^* \rangle$, respectively. Likewise in figure 11, a comparison between the figures 13a to 13c highlights a different trend in case of the cooled wall, as in the viscous sub-layer the quantities v' and T' are weakly anti-correlated while they exhibit a subtle correlation for the other two cases (A and H). For case C, on moving towards higher y^+ , we see that at $y^+ = 10$, the major axis of the JPDP contours becomes parallel to the v' axis and the distribution becomes flat, and the peak of the contours remains close to the origin. However, in the log region, figures 13g and 13j, the major axis of the contours aligns itself in the Q_1 and Q_3 in an anti-clockwise sense which means that more amount of fluid is going towards the wall. This set of figures shows that for the adiabatic and the heated walls, the quantities v' and T' show correlation from the viscous sublayer itself. This means that the effects of temperature on the turbulent boundary layers can be seen from the viscous sublayer to the buffer-layer region. Afterwards, for $y^+ \geq 35$, as a result of the turbulent mixing, the

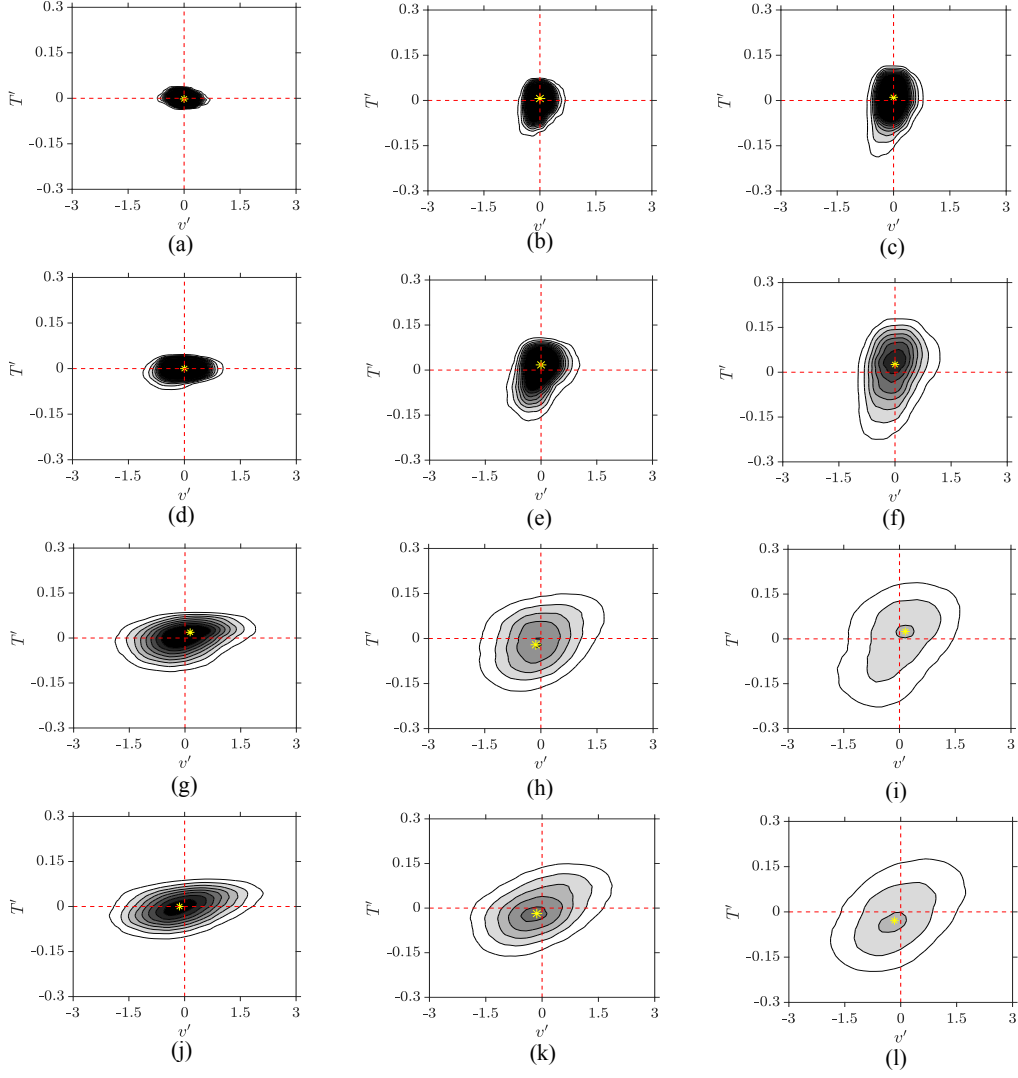


Figure 13: Contours of the JPDF distribution of the v' and T' for $y^+ = 5$ ((a)-(c)), 10 ((d)-(f)), 35 ((g)-(i)) and 90 ((j)-(l)). Here the first, second and third columns represent the cooled, adiabatic and heated walls, respectively. The color of the contour levels vary from 40 to 320 (light to dark).

608 differences arising from the wall-temperature are not so significant in terms
 609 of the peak position, but the maximum value of the JPDF contours does
 610 decrease with increasing wall-temperature.

611 We would now discuss about the contour plots of the covariance integrand
 612 of the v' and T' i.e. $v'T'P(v',T')$ in order to reveal the contributions of
 613 different physical phenomena towards the turbulent wall-normal heat-flux
 614 covariance, $\overline{v'T'}$. Following quadrant analysis is presented for the $v'T'$ plane.
 615 The first quadrant (Q_1), with $v' > 0$ and $T' > 0$, indicates that the heated
 616 fluid is moving away from the wall. The second quadrant (Q_2), where $v' < 0$
 617 and $T' > 0$, means that the heated fluid moving down towards the wall. The
 618 third quadrant (Q_3), with $v' < 0$ and $T' < 0$, highlights the events where
 619 cooled fluid moves towards the wall while the fourth quadrant (Q_4), with
 620 $v' > 0$ and $T' < 0$, indicates the events of the cooled fluid moving away from
 621 the wall. The contours of the covariance integrands of the v' and T' are shown
 622 in figure 14 for all the cases at different y^+ locations. Like before, the white
 623 region surrounding the gray rectangles represents the region with no data. It
 624 should be noted here that in order to have a clear representation, figure 14a,
 625 and figures 14b and c are zoomed-in by four and two times respectively for
 626 both the axes with reference to the planes' dimensions used for figures 14d
 627 to l. It can be seen in figure 14 that for all the cases the Q_1 and Q_3 are the
 628 dominant quadrants except for figure 14a where the Q_2 and Q_4 are dominant.
 629 In the viscous sub-layer, at $y^+ = 5$, it can be seen that for the cooled wall, the
 630 Q_2 is more dominant in comparison to the Q_4 which means that the heated
 631 fluid is going towards the wall has more contribution towards the turbulent
 632 wall-normal heat-flux which is the reason why the wall is behaving as the

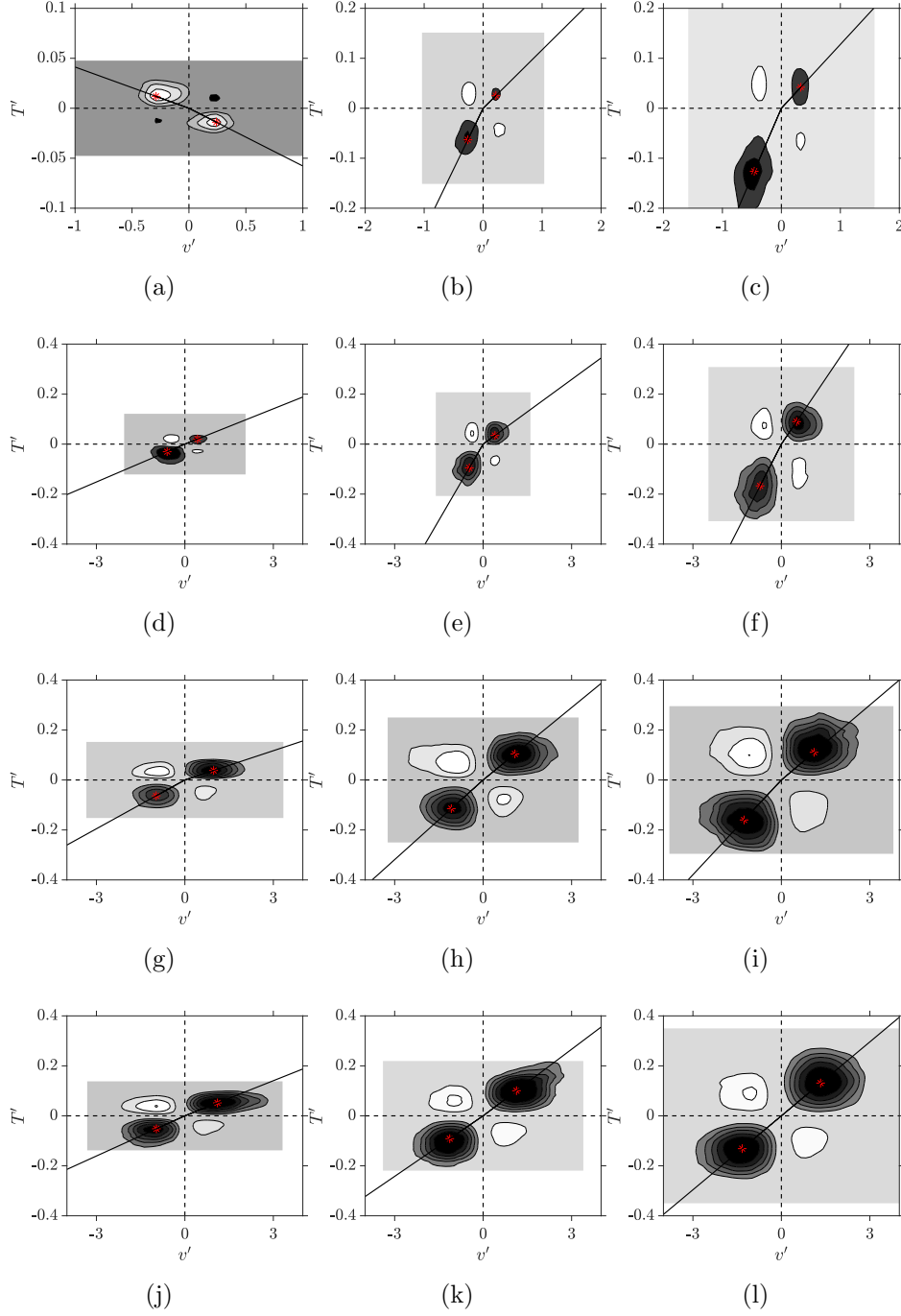


Figure 14: Contours of the covariance integrands of the v' and T' at $y^+ = 5$ ((a)-(c)), 10 ((d)-(f)), 35 ((g)-(i)) and 90 ((j)-(l)). Here, the first, second and third columns represent the cooled, adiabatic and heated walls, respectively. The colors of the contour levels vary from -2.5 to 1, excluding the zero level (light to dark) for (a), from -1 to 1, excluding the zero level for (d) and from -3 to 6 for the rest.

633 heat sink here, as pointed out by Lechner et al. [22]. On the other hand,
 634 for the adiabatic and the heated cases, at the same y^+ location (figures 14b
 635 and 14c), the Q_3 is more dominant in comparison to the Q_1 which means
 636 that the cooled fluid moving towards the wall is the major contributor to the
 637 turbulent wall-normal heat-flux. Therefore, in these cases, the wall is acting
 638 as a heat source. In the buffer layer, $y^+ = 10$, the Q_3 is more dominant than
 639 the Q_1 irrespective of the wall temperature. From figures 14g-l, it can be seen
 640 that in the log region from $y^+ = 35$ to 90, the Q_1 is more dominant than the
 641 Q_3 for all of the cases highlighting that the principal contribution is coming
 642 from the events of the Q_1 than the events of the Q_3 . From the observations
 643 drawn from this set of figures, it can be concluded that the wall-cooling
 644 has significant effect on the heat-transfer mechanisms for the compressible
 645 turbulent boundary layer which is clearly highlighted in the near-wall region
 646 (up to $y^+ = 5$). In the higher y^+ regions, the physical mechanisms responsible
 647 for the heat-transfer do not change significantly with the wall-temperature,
 648 but slight variations in their amplitudes are registered. This explains the
 649 difference in the levels of the wall-normal Reynolds heat-flux observed for
 650 the heated and the cooled walls found by Sharma et al. [29].

651 **5. Conclusion**

652 Direct numerical simulations (DNS) for the supersonic boundary layers
 653 (SBLs) with free-stream Mach number of $M_\infty = 2.2$ were carried out. Three
 654 DNS test cases were investigated in order to unravel the effects of the wall-
 655 temperature on the turbulent flow topology for the SBLs. **The implications**
 656 **on the important physical parameters like the turbulent shear-stress, the**

657 orientation of the projections of the coherent structures in different planes,
658 and different components of the turbulent heat-flux were analyzed using the
659 joint probability density function (JPDF) distribution and the covariance
660 integrands' analyses.

661 The results showed that the sweeps were the dominant physical phe-
662 nomenon majorly contributing to the turbulent shear-stress in the buffer
663 layer. But, for the heated wall, both the ejections and the sweeps became
664 comparable transfer processes. In the log-region, ejections had the domi-
665 nant contribution to the shear-stress irrespective of the wall-temperature.
666 These trends showed similarities with the findings reported by Wallace et al.
667 [8], Ong and Wallace [11] regarding the adiabatic incompressible boundary
668 layers. The results presented also highlighted different trends for the angles
669 of inclination (α and β) of the projections of the coherent structures in case
670 of the heated wall, as a result of the increased heat transfer from the sur-
671 face of the wall. The trends of α and β showed good agreement with the
672 compressible and the incompressible counterparts reported in the literature.

673 The plots of the covariance integrands of the u' and T' showed that for the
674 adiabatic and the heated walls, the Q_2 and Q_4 were the dominant quadrants
675 implying the principal contribution of the fast moving cooled fluid towards
676 the streamwise turbulent wall heat-transfer extending from the viscous sub-
677 layer to the log-region. Whereas for the cooled wall, the Q_1 and Q_3 were
678 found to be the major contributors in the viscous sub-layer. A similar con-
679 trasting trend was observed for the cooled wall again, for the wall-normal
680 component of the turbulent heat-flux in the viscous sub-layer where the Q_2
681 had dominance in comparison to the Q_4 , meaning that heated fluid going

682 towards the wall had more contribution towards the turbulent wall-normal
683 heat-flux. For the rest, the Q_1 and Q_3 were the dominant quadrants.

684 6. Acknowledgements

685 This work was granted access to HPC resources of IDRIS under the allo-
686 cation 2017-100752 made by GENCI (Grand Equipement National de Calcul
687 Intensif- A0022A10103). The authors acknowledge the access to HPC re-
688 sources of French regional computing center of Normandy named CRIANN
689 (Centre Régional Informatique et d'Applications Numériques de Normandie)
690 under the allocations 1998022 and 2017002. The funding resources provided
691 from European projects entitled FEDER and NEPTUNE 1 are gratefully
692 acknowledged. Authors would also like to extend their gratitude to both the
693 reviewers whose critical comments helped us to substantially improve the
694 quality of the paper.

695 7. References

- 696 [1] K. Bensayah, A. Hadjadj, A. Bounif, Heat transfer in turbulent bound-
697 ary layers of conical and bell shaped rocket nozzles with complex wall
698 temperature, Numerical Heat Transfer, Part A: Applications 66 (2014)
699 289–314.
- 700 [2] L. Duan, I. Beekman, M. Martin, Direct numerical simulation of hy-
701 personic turbulent boundary layers. part 2. effect of wall temperature,
702 Journal of Fluid Mechanics 655 (2010) 419–445.
- 703 [3] T. Theodorsen, Mechanisms of turbulence, in: Proceedings of the 2nd
704 Midwestern Conference on Fluid Mechanics, 1952.

- 705 [4] M. Head, P. Bandyopadhyay, New aspects of turbulent boundary-layer
706 structure, *Journal of fluid mechanics* 107 (1981) 297–338.
- 707 [5] M. Stanislas, L. Perret, J.-M. Foucaut, Vortical structures in the tur-
708 bulent boundary layer: a possible route to a universal representation,
709 *Journal of Fluid Mechanics* 602 (2008) 327–382.
- 710 [6] X. Wu, P. Moin, Direct numerical simulation of turbulence in a nomi-
711 nally zero-pressure-gradient flat-plate boundary layer, *Journal of Fluid*
712 *Mechanics* 630 (2009) 5–41.
- 713 [7] E. R. Corino, R. S. Brodkey, A visual investigation of the wall region in
714 turbulent flow, *Journal of Fluid Mechanics* 37 (1969) 1–30.
- 715 [8] J. M. Wallace, H. Eckelmann, R. S. Brodkey, The wall region in turbu-
716 lent shear flow, *Journal of Fluid Mechanics* 54 (1972) 39–48.
- 717 [9] J. M. Wallace, R. S. Brodkey, Reynolds stress and joint probability
718 density distributions in the u-v plane of a turbulent channel flow, *The*
719 *Physics of Fluids* 20 (1977) 351–355.
- 720 [10] W. Willmarth, S. Lu, Structure of the reynolds stress near the wall,
721 *Journal of Fluid Mechanics* 55 (1972) 65–92.
- 722 [11] L. Ong, J. M. Wallace, Joint probability density analysis of the structure
723 and dynamics of the vorticity field of a turbulent boundary layer, *Journal*
724 *of Fluid Mechanics* 367 (1998) 291–328.
- 725 [12] A.-T. Le, G. N. Coleman, J. Kim, Near-wall turbulence structures in

- 726 three-dimensional boundary layers, *International journal of heat and*
727 *fluid flow* 21 (2000) 480–488.
- 728 [13] P. Bechlars, R. Sandberg, Variation of enstrophy production and strain
729 rotation relation in a turbulent boundary layer, *Journal of Fluid Me-*
730 *chanics* 812 (2017) 321–348.
- 731 [14] P. Bechlars, R. Sandberg, Evolution of the velocity gradient tensor
732 invariant dynamics in a turbulent boundary layer, *Journal of Fluid*
733 *Mechanics* 815 (2017) 223–242.
- 734 [15] E. F. Spina, A. J. Smits, S. K. Robinson, The physics of supersonic
735 turbulent boundary layers, *Annual Review of Fluid Mechanics* 26 (1994)
736 287–319.
- 737 [16] M. V. Morkovin, Effects of compressibility on turbulent flows,
738 *Mécanique de la Turbulence* 367 (1962) 380.
- 739 [17] A. J. Smits, J.-P. Dussauge, *Turbulent shear layers in supersonic flow*,
740 Springer Science & Business Media, 2006.
- 741 [18] W. Li, L. Xi-Yun, Statistical analysis of coherent vortical structures in a
742 supersonic turbulent boundary layer, *Chinese Physics Letters* 28 (2011)
743 034703.
- 744 [19] T. Maeder, N. A. Adams, L. Kleiser, Direct simulation of turbulent
745 supersonic boundary layers by an extended temporal approach, *Journal*
746 *of Fluid Mechanics* 429 (2001) 187–216.

- 747 [20] S. Pirozzoli, F. Grasso, T. Gatski, Direct numerical simulation and
748 analysis of a spatially evolving supersonic turbulent boundary layer at
749 $M = 2.25$, *Physics of fluids* 16 (2004) 530–545.
- 750 [21] S. Pirozzoli, M. Bernardini, F. Grasso, Characterization of coherent
751 vortical structures in a supersonic turbulent boundary layer, *Journal of*
752 *Fluid Mechanics* 613 (2008) 205–231.
- 753 [22] R. Lechner, J. r. Sesterhenn, R. Friedrich, Turbulent supersonic channel
754 flow, *Journal of Turbulence* 2 (2001) 001–001.
- 755 [23] M. Shadloo, A. Hadjadj, F. Hussain, Statistical behavior of supersonic
756 turbulent boundary layers with heat transfer at $M_\infty = 2$, *International*
757 *Journal of Heat and Fluid Flow* 53 (2015) 113–134.
- 758 [24] A. Trettel, J. Larsson, Mean velocity scaling for compressible wall tur-
759 bulence with heat transfer, *Physics of Fluids* 28 (2016) 026102.
- 760 [25] A. Patel, B. J. Boersma, R. Pecnik, Scalar statistics in variable property
761 turbulent channel flows, *Physical Review Fluids* 2 (2017) 084604.
- 762 [26] Y.-B. Chu, Y.-Q. Zhuang, X.-Y. Lu, Effect of wall temperature on
763 hypersonic turbulent boundary layer, *Journal of Turbulence* 14 (2013)
764 37–57.
- 765 [27] M. S. Shadloo, A. Hadjadj, D. J. Bodony, F. Hussain, S. K. Lele, Effects
766 of heat transfer on transitional states of supersonic boundary layers,
767 in: *Proceedings of Summer program, Center of Turbulence Research,*
768 *Stanford University, USA*, pp. 175–184.

- 769 [28] M. Shadloo, A. Hadjadj, Laminar-turbulent transition in supersonic
770 boundary layers with surface heat transfer: A numerical study, Numer-
771 ical Heat Transfer, Part A: Applications (2017) 1–14.
- 772 [29] S. Sharma, M. Shadloo, A. Hadjadj, Laminar-to-turbulent transition
773 in supersonic boundary layer: Effects of initial perturbation and wall
774 heat-transfer, Numerical Heat Transfer, Part A: Applications (2018)
775 doi:10.1080/10407782.2018.1464785.
- 776 [30] A. Chaudhuri, A. Hadjadj, A. Chinnayya, S. Palerm, Numerical study
777 of compressible mixing layers using high-order weno schemes, Journal
778 of Scientific Computing 47 (2011) 170–197.
- 779 [31] G.-S. Jiang, C.-W. Shu, Efficient implementation of weighted eno
780 schemes, Journal of computational physics 126 (1996) 202–228.
- 781 [32] A. Chaudhuri, A. Hadjadj, O. Sadot, E. Glazer, Computational study
782 of shock-wave interaction with solid obstacles using immersed boundary
783 methods, International Journal for Numerical Methods in Engineering
784 89 (2012) 975–990.
- 785 [33] D. Ngomo, A. Chaudhuri, A. Chinnayya, A. Hadjadj, Numerical study
786 of shock propagation and attenuation in narrow tubes including friction
787 and heat losses, Computers & Fluids 39 (2010) 1711–1721.
- 788 [34] O. Ben-Nasr, A. Hadjadj, A. Chaudhuri, M. Shadloo, Assessment of
789 subgrid-scale modeling for large-eddy simulation of a spatially-evolving
790 compressible turbulent boundary layer, Computers & Fluids (2016).

- 791 [35] L. M. Mack, Boundary-layer linear stability theory, Technical Re-
792 port, CALIFORNIA INST OF TECH PASADENA JET PROPULSION
793 LAB, 1984.
- 794 [36] F. M. White, I. Corfield, Viscous fluid flow, volume 3, McGraw-Hill New
795 York, 2006.
- 796 [37] K. Masatsuka, I do like cfd, Published by Katate Masatsuka (2009).
- 797 [38] S. Sharma, M. S. Shadloo, A. Hadjadj, Laminar-to-turbulent transition
798 in supersonic boundary layer: Effects of initial perturbation and wall
799 heat transfer, Numerical Heat Transfer, Part A: Applications 73 (2018)
800 583–603.
- 801 [39] S. Sharma, M. Shadloo, A. Hadjadj, Effect of thermo-mechanical non-
802 equilibrium on the onset of transition in supersonic boundary layers,
803 Heat and Mass Transfer (2018) 1–13.